Title

Structure of Hsp90-Hsp70-Hop-GR reveals the Hsp90 client-loading mechanism.

Permalink

https://escholarship.org/uc/item/57d1j045

Journal

Nature: New biology, 601(7893)

Authors

Wang, Ray

Noddings, Chari

Kirschke, Elaine

et al.

Publication Date

2022

DOI

10.1038/s41586-021-04252-1

Peer reviewed

Structure of Hsp90–Hsp70–Hop–GR reveals the Hsp90 client-loading mechanism

Ray Yu-Ruei Wang[1], **Chari M. Noddings**[1], **Elaine Kirschke**[1], **Alexander G. Myasnikov**[1,3], **Jill L. Johnson**[2], **David A. Agard**[1,✉]

[1]Department of Biochemistry and Biophysics, University of California San Francisco, San Francisco, CA, USA

[2]Department of Biological Sciences, University of Idaho, Moscow, ID, USA

[3]Present address: Dubochet Center for Imaging (DCI) at EPFL, EPFL SB IPHYS DCI, Lausanne, Switzerland

Abstract

Maintaining a healthy proteome is fundamental for the survival of all organisms[1]. Integral to this are Hsp90 and Hsp70, molecular chaperones that together facilitate the folding, remodelling and maturation of the many 'client proteins' of Hsp90[2]. The glucocorticoid receptor (GR) is a model client protein that is strictly dependent on Hsp90 and Hsp70 for activity[3–7]. Chaperoning GR involves a cycle of inactivation by Hsp70; formation of an inactive GR–Hsp90–Hsp70–Hop 'loading' complex; conversion to an active GR–Hsp90–p23 'maturation' complex; and subsequent GR release[8]. However, to our knowledge, a molecular understanding of this intricate chaperone cycle is lacking for any client protein. Here we report the cryo-electron microscopy structure of the GR-loading complex, in which Hsp70 loads GR onto Hsp90, uncovering the molecular basis of direct coordination by Hsp90 and Hsp70. The structure reveals two Hsp70 proteins, one of which delivers GR and the other scaffolds the Hop cochaperone. Hop interacts with all components of the complex, including GR, and poises Hsp90 for subsequent ATP hydrolysis. GR is partially unfolded and recognized through an extended binding pocket composed of Hsp90, Hsp70 and Hop, revealing the mechanism of GR loading and inactivation. Together with the GR-maturation complex structure[9], we present a complete molecular mechanism of chaperone-

dependent client remodelling, and establish general principles of client recognition, inhibition, transfer and activation.

The highly abundant and conserved Hsp90 and Hsp70 molecular chaperones are essential for proteome maintenance. Hsp70 recognizes virtually all unfolded or misfolded proteins, and generally functions early in protein folding[10]. By contrast, Hsp90 typically functions later, and targets a select set of 'client' proteins[11]. Despite the differences, Hsp90 and Hsp70 share clients that are highly enriched for signalling and regulatory proteins[2], making both chaperones important pharmaceutical targets for cancer[12] and neurodegenerative diseases[13]. Both chaperones are dynamic molecular machines with complex ATP-dependent conformational cycles that drive the binding and release of clients. Hsp70 uses its N-terminal nucleotide-binding domain ($Hsp70_{NBD}$) to allosterically regulate its C-terminal substrate-binding domain ($Hsp70_{SBD}$), which comprises a β-sandwich core ($Hsp70_{SBD-\beta}$) and an α-helical lid ($Hsp70_{SBD-\alpha}$)[14] (Extended Data Fig. 1a). In the weak client-binding ATP-bound 'open' state ($Hsp70^{ATP}$), both the $Hsp70_{SBD-\alpha}$ and the $Hsp70_{SBD-\beta}$ dock onto the $Hsp70_{NBD}$. After ATP hydrolysis ($Hsp70^{ADP}$), the $Hsp70_{NBD}$ and $Hsp70_{SBD}$ subdomains separate, resulting in a high-affinity client-binding state. Hsp90 constitutively dimerizes through its C-terminal domain ($Hsp90_{CTD}$) (Extended Data Fig. 1a) and cycles through open and closed conformations acting as a molecular clamp[15,16]. In the nucleotide-free state ($Hsp90^{Apo}$), Hsp90 populates a variety of open conformations, whereas ATP binding ($Hsp90^{ATP}$) drives clamp closure through secondary dimerization of the N-terminal domains ($Hsp90_{NTD}$). Clamp closure activates Hsp90 for ATP hydrolysis and is rate-limiting, requiring $Hsp90_{NTD}$ rotation, N-terminal helix rotation and closure of the lid of the ATP-binding pocket. Unlike Hsp70, Hsp90 can engage clients independently of nucleotide state through the middle domain ($Hsp90_{MD}$) and the amphipathic helix-hairpins ($Hsp90_{amphi-\alpha}$ on the $Hsp90_{CTD}$[16]

The glucocorticoid receptor (GR) is a steroid-hormone-activated transcription factor that constitutively depends on Hsp90 to function[4,5]. Building on the work of others[6,7] we previously reconstituted the Hsp90 dependence of GR using an in vitro system[8], and established a four-step cycle (Fig. 1a) that starts with the active GR ligand-binding domain (hereafter, GR for simplicity). Next, Hsp70 inactivates GR ligand binding, and then the cochaperone Hop (Hsp90–Hsp70 organizing protein) helps to load Hsp70–GR onto Hsp90, forming the inactive 'client-loading' complex (GR–Hsp90–Hsp70–Hop). After Hsp90 ATP hydrolysis and closure, Hsp70 and Hop are released, followed by the incorporation of p23, forming the GR–Hsp90–p23 'client-maturation' complex. In the maturation complex, GR is reactivated, indicating that GR is conformationally remodelled during the transition. A similar pattern of Hsp70 and Hsp90 functional antagonism has subsequently been shown for other clients[17–19], supporting a general mechanism.

The molecular basis for almost all of this complex chaperone interplay remains unknown, with high-resolution structural studies hampered by the instability of client proteins and the highly dynamic nature of client-chaperone associations. Here we report a high-resolution cryo-electron microscopy (cryo-EM) structure of the client-loading complex, which provides molecular insights into how Hsp90 and Hsp70 coordinate their ATP cycles, how they are

organized by Hop, and the molecular mechanisms that underlie the functional regulation of GR by Hsp90 and Hsp70.

Architecture of the GR-loading complex

The client-loading complex was prepared by reconstitution using excess ADP to enhance client binding by Hsp70 and an ATP-binding deficient Hsp90 (Hsp90(D93N)) to stall the cycle at this intermediate step, followed by glutaraldehyde stabilization (Extended Data Fig. 1b, c). A cryo-EM reconstruction at around 3.6 Å resolution was obtained from about 4 million particles (Extended Data Figs. 1d–f, 2, Methods). The resulting structure reveals an architecture markedly different to that expected, with the Hsp90 dimer (Hsp90A/B) surrounded by Hop, GR and two Hsp70s (Hsp70'C' for client-loading and Hsp70'S' for scaffolding) (Fig. 1b, c). Hsp90 adopts a 'semi-closed' conformation, in which the $Hsp90_{NTD}s$ have rotated into an $Hsp90^{ATP}$-like orientation, but have not yet reached the fully closed ATP state (Extended Data Fig. 3b, c). The observed $Hsp90_{NTD}$ orientations are stabilized by the $Hsp70_{NBD}s$ that bind symmetrically to the $Hsp90_{NTD}$–$Hsp90_{MD}$ interface of each Hsp90 protomer. Hop intimately interacts with each Hsp90 protomer, the two Hsp70s and, notably, a portion of GR. Although the two $Hsp70_{SBD}s$ are not visible in the high-resolution map, the $Hsp70C_{SBD-\beta}$ subdomain becomes visible in low-pass-filtered maps (Fig. 1b). Also seen in the filtered maps, GR is positioned on one side of the Hsp90 dimer (Fig. 1c). In addition, another map (around 7 Å) reveals a loading complex that has lost Hsp70C but that retains Hsp70S, Hop and GR (Extended Data Fig. 3d, e). The observation of the two-Hsp70 and one-Hsp70 loading complexes populated in our sample is consistent with a previous study[20].

The ATP-regulated Hsp90–Hsp70 interplay

Two major interfaces (Fig. 1d) are formed in both of the nearly identical $Hsp70_{NBD}$–Hsp90 protomer interactions (root mean square deviation (RMSD) of 0.96 Å) (Supplementary Fig. 1a–c). In interface I, the outer edge of the $Hsp90_{MD}$ β-sheet inserts into the cleft formed by the $Hsp70_{NBD-IA}$ and $Hsp70_{NBD-IIA}$ subdomains (Fig. 1d, Extended Data Fig. 4a). Of note, in $Hsp70^{ATP}$ this cleft binds the Hsp70 interdomain linker and also contributes to binding to the Hsp40 J-domain[14] (Extended Data Fig. 4b). Hence, the cleft is only available for Hsp90 in $Hsp70^{ADP}$. Interface I is tightly packed (approximately 479 $Å^2$ of buried surface area; BSA), and is stabilized by numerous polar interactions (Fig. 1d, e). This explains why mutations at interface I on either Hsp90 (G333, K414, K418, K419)[21–23] or Hsp70 (R171, N174, D213)[24] led to defective Hsp90-Hsp70 interaction, growth defects and impaired client maturation of GR, v-Src and luciferase (Fig. 1d, e, Extended Data Fig. 4c–h; see Supplementary Table 3 for equivalent yeast residue numbering).

The two ATPase domains of Hsp90 and Hsp70 directly interact with each other at interface II (Fig. 1d, f, approximately 280 $Å^2$ BSA), using a combination of hydrophobic (Hsp90(Y61, L64)–Hsp70(V163, I164)) and polar contacts (Hsp90(R60, Y61)–Hsp70(D160)). Notably, interface II defines the $Hsp90^{ATP}$-like position and orientation of the $Hsp90_{NTD}$ with respect to the $Hsp90_{MD}$, explaining the observation that Hsp70 accelerates Hsp90 ATPase activity[25]. Consistent with the significance of interface II,

mutation of the three Hsp90 interface residues (Hsp90 R60, Y61 and L64) resulted in marked yeast growth defects at 37 °C (ref. [26]). Similar to the interface I mutations G333S and K418E in Hsp90 (G309S and K394E in yeast Hsc82), an Hsp90 mutation at R60 (yHsc82(R46G)) led to reduced Hsp70 interaction, inviability at 37 °C and reduced v-Src activity (Extended Data Fig. 4e–h). Finally, sequence alignments of Hsp90 and Hsp70 homologues and paralogues showed that interface I and II residues are generally conserved, suggesting a universal Hsp90–Hsp70 binding strategy across species[23,24,27] and organelles[28,29] (Supplementary Fig. 2a, b).

As expected from Hsp90(D93N), both $Hsp90_{NTD}$ ATP-binding pockets are empty with their lids open. The $Hsp90A_{NTD}$ and $Hsp90B_{NTD}$ closely resemble the structure of an apo-$Hsp90_{NTD}$ fragment (RMSD of 0.43 and 0.35 Å to Protein Data Bank (PDB) ID 3T0H, respectively) (Extended Data Fig. 5a). The ATP pocket lid and the first α-helix form a dimerization interface (approximately 512 $Å^2$ BSA) (Extended Data Fig. 3a). The two $Hsp70_{NBD}$s clearly have ADP bound and are similar to the ADP-bound $Hsp70_{NBD}$ crystal structure (Cα-RMSD of 0.50 Å (Hsp70C) and 0.53 Å (Hsp70S) to PDB ID 3AY9) (Fig. 1d, Supplementary Fig. 3a, b).

Coordination between the Hsp90 and Hsp70 ATPase cycles is required for forming the loading complex. The $Hsp90^{ATP}$ conformation is incompatible as closure of the $Hsp90^{ATP}$ ATP pocket lid and the central helix of $Hsp90_{NTD}$ would clash with the $Hsp70_{NBD}$ (Extended Data Fig. 5b, c). Thus, Hsp90 ATP binding and lid closure would be expected to accelerate loss of the bound Hsp70s. Furthermore, the $Hsp70^{ATP}$ conformation is incompatible with the loading complex, as the entire $Hsp70_{SBD}$ would clash with $Hsp90_{NTD}$–$Hsp90_{MD}$ (Extended Data Fig. 5d, e). For Hsp70 to re-enter its ATP cycle, it must first leave Hsp90, thus nucleotide exchange on Hsp70 is likely to time its dissociation. Of note, in the loading complex, $Hsp70_{NBD-IIA}$s deviate from the crystal structure (Supplementary Fig. 3a, b) and $Hsp90_{MD}$ interacts with Hsp70 (R171, N174, T177) in the ATP catalytic motif (Fig. 1e, Supplementary Fig. 3c), suggesting how Hsp90 enhances the nucleotide exchange on Hsp70 during the GR-chaperoning cycle[30]. The canonical nucleotide exchange factor (NEF)-binding sites[10,14] on $Hsp70_{NBD-IIB}$ remain available, explaining how the NEF Bag-1 can accelerate GR maturation[30] (Supplementary Fig. 4a, b) and also how the NEF Hsp110 can be involved in GR maturation[31] (Supplementary Fig. 4c, d).

Hop binds to all complex components

The cochaperone Hop is well-conserved in eukaryotes and facilitates GR maturation in vivo[32] and in vitro[8]. Hop is thought to bring Hsp90 and Hsp70 together using its three tetratricopeptide repeat (TPR) domains that bind the EEVD C termini on both Hsp90 and Hsp70[33] (Extended Data Fig. 1a). Despite using the full-length Hop construct, only the three C-terminal domains (Hop_{TPR2A}, Hop_{TPR2B} and Hop_{DP2}) are observed (Fig. 1b, c). Notably, these three domains are necessary and sufficient for full GR activation[33]. Hop wraps around much of the loading complex, with extensive interactions made by Hop_{TPR2A} and Hop_{DP2}, demonstrating a far more integral role than was anticipated (Fig. 2a, c).

The structure of Hop$_{TPR2A-TRP2B}$ closely matches the yeast crystal structure[33] (Cα-RMSD of 1.47 Å to PDB ID 3UQ3, Supplementary Fig. 5a, c, d), including the conserved electrostatic network (Hop(Y354, R389, E385, K388)) that defines the unique interdomain angle (Supplementary Fig. 5h–j). Focused maps revealed that Hop$_{TPR2A}$ and Hop$_{TPR2B}$ are bound to the EEVD termini of Hsp90 and Hsp70, respectively (Extended Data Fig. 6d–f, Supplementary Fig. 6b–f, k, l). Although the density for the remaining Hsp70 and Hsp90 tails is missing, our structural modelling suggested the connectivity (Supplementary Fig. 7a, b). Hop$_{TPR2A}$ and Hsp70S$_{NBD-IIA}$ form an extensive interface (approximately 578 Å^2 BSA) composed largely of polar interactions (Fig. 2a, b, Extended Data Fig. 6a–d, g). Hsp70S$_{NBD-IIA}$ interacts with Hop and Hsp90 simultaneously, thereby rigidly positioning Hop with respect to Hsp90. Y296A–A328H mutations of Hop (Y332–T364 in yeast, Sti1) at the Hsp70S$_{NBD-IIA}$–Hop$_{TPR2A}$ interface (Extended Data Fig. 6a–c, g) resulted in yeast growth defects (Extended Data Fig. 6i) and did not promote v-Src maturation (Extended Data Fig. 6j). These data indicate that Hsp70S has a crucial scaffolding role in the loading complex. Although Hop$_{TPR2B}$ was in close proximity (around 6 Å) to Hsp90$_{MD}$, no major contacts were observed (Fig. 2c). However, the 15-Å-resolution Hsp90–Hop cryo-EM structure[34] (Supplementary Fig. 7c) and previous studies[33,35] show that Hop$_{TPR2B}$ can make direct contacts with Hsp90$_{MD}$. This suggests that Hop may first prepare Hsp90 for Hsp70 and client interaction, and subsequently rearrange after Hsp70S$_{NBD}$ binding (Supplementary Fig. 7d, e).

Hop$_{DP2}$ makes extensive interactions with both Hsp90 protomers at Hsp90A$_{CTD}$ and Hsp90B$_{MD}$, thereby defining and maintaining the semi-closed Hsp90 conformation within the loading complex (Fig. 3a). This poises Hsp90 for the subsequent fully closed ATP conformation. Notably, conserved client-binding residues on Hsp90 are repurposed for Hop$_{DP2}$ binding (Fig. 2d, Extended Data Fig. 8a). Supporting our observations, Hsp90 mutations (yHsp82 W585T and M593T, corresponding to hHsp90α W606 and M614) that would destabilize the Hop$_{DP2}$–Hsp90A interface (Fig. 2d) cause yeast growth defects[36]. Our Hop$_{DP2}$ structure agrees well with the yeast nuclear magnetic resonance (NMR) structure[33] (Cα-RMSD of 1.13 Å to PDB 1D 2LLW) (Supplementary Fig. 5b), adopting a hand-like α-helical structure, with many of its core hydrophobic sidechains exposed in the 'palm' of the 'hand' (Fig. 3d, Extended Data Fig. 8a). This hydrophobic palm is continuous with the client-binding surface provided by the lumen between the Hsp90 protomers, augmenting the Hsp90A$_{amphi-α}$ with a stronger, more-extensive hydrophobic binding capability (Fig. 3a).

Unfolded GR is bound by Hsp90–Hop–Hsp70

In the high-resolution map, a strand of density can be seen passing through the Hsp90 lumen (Extended Data Fig. 7a–c). In the 10 Å low-pass-filtered map, this density connects to the globular part of GR on one side of Hsp90 (Fig. 1c, Extended Data Fig. 7e, f). On the other side, a GR helix is cradled in the Hop$_{DP2}$ hydrophobic palm and the rest of GR becomes a strand embedded in the Hsp70C$_{SBD-β}$ substrate-binding pocket (Fig. 3a–d, Extended Data Figs. 8b, 9d, Supplementary Figs. 8a, b, 9d–f). Thus, GR is partially unfolded and threaded through the Hsp90 lumen. This client-unfolding on Hsp90 is reminiscent of how the unfolded CDK4 kinase was captured by Hsp90[37], although via the fully closed Hsp90^{ATP}. To test this client–cochaperone interaction, we substituted the Hop residue Q512

in Hop_{DP2} (which is close to, but not directly interacting with, the GR helix) with the photoreactive unnatural amino acid *p*-benzoyl-phenylalanine (Extended Data Fig. 8b–d). In support of our structure, GR and Hop become photo-cross-linked (Extended Data Fig. 8c, d). In addition, a residue in the Hop_{DP2} hydrophobic palm (Hop L508; L553 in yeast, Sti1) that directly interacts with GR (Figs. 2d, 3d, Extended Data Fig. 8e) is functionally important. Mutations of this residue decrease yeast viability (Hop(L508D)) (Extended Data Fig. 8g), and completely abrogate the function of GR (Hop(L508A); ref. [33]) and v-Src (Hop(L508D)) (Extended Data Fig. 8h) in vivo. These data indicate that client binding to Hop_{DP2} is crucial for both general cellular function and protein maturation across different Hsp90 client systems.

We next sought to determine which GR segment is captured in the loading complex lumen. The GR maturation complex structure unambiguously demonstrates that GR's pre-helix 1 strand ($GR^{523–531}$, $GR_{pre-Helix1}$) is gripped in the closed Hsp90 lumen[9]. Re-examination of previous Hsp70-GR hydrogen deuterium exchange mass spectrometry (HDX-MS) data[8] reveals that only $GR_{pre-Helix1}$ becomes protected upon Hsp70 binding (Extended Data Fig. 9a,b) and $GR_{pre-Helix1}$ also contains high-scoring predicted Hsp70-binding sites ($GR^{519–526}$) (Extended Data Fig. 9a). This strongly supports a model in which Hsp70 first inhibits GR by capturing $GR_{pre-Helix1}$. Then, Hsp70 loads GR onto Hsp90–Hop with $GR_{pre-Helix1}$ bound, forming the client-loading complex (Extended Data Fig. 9b–d). This model was tested by incorporating the photoreactive cross-linker at two positions in the $GR_{pre-Helix1}$ residues either before (GR^{517}) or after (GR^{527}) the predicted Hsp70-binding site (Extended Data Fig. 10a). As expected, at both positions, cross-links between GR and Hsp70 were formed in the loading complex (Extended Data Fig. 10b, c). In addition, both positions were able to cross-link with Hop (Extended Data Fig. 10b, c), indicating that it is Hsp70C that the $GR_{pre-Helix1}$ cross-linked with, rather than Hsp70S. Consistent with our model, a previous optical-tweezer study[38] showed that GR_{Helix1} is readily detached, correlating with ligand binding loss. Together, this indicates that perturbations to GR_{Helix1} by Hsp70 or the loading complex leads to loss of GR ligand binding, explaining the inactivation of GR during the chaperone cycle.

Despite extensive 3D classifications, the main body of GR remained at low resolution. Nonetheless, the $Hsp90_{MDS}$ from each protomer and the $Hsp90B_{amphi-α}$ clearly contact GR (Extended Data Fig. 7b–d, f, g). Hsp90 residues previously found[21,22,39–41] to affect GR maturation are highlighted in Fig. 3e. The exposed Hsp90A(W320, F349) directly contact GR in both the loading complex (Fig. 3e, Extended Data Fig. 7g), and the maturation complex[9]. Notably, Hsp90 W320 (W300 in yHsp82) is an important binding residue that is exploited by both clients and cochaperones. Not only does it interact with GR and Hop_{DP2} (Fig. 2d), but it also interacts with another cochaperone, Aha1[42]. Supporting its broad functional importance, numerous studies have reported deleterious effects of Hsp90 W320 mutations on GR activation[40,43] and yeast growth[26].

Discussion

Our client-loading complex structure provides a view of how Hsp70, Hsp90 and Hop work together to chaperone a client. Several features were unexpected. (1) Two Hsp70s

bind the Hsp90 dimer–one delivers client and the second scaffolds Hop. (2) Hop interacts extensively with all components, including GR, going well beyond the anticipated TPR-EEVD interactions. (3) Together, Hop–Hsp90 and Hsp70–Hsp90 interactions define the Hsp90 conformation, poising it both for client binding and ultimately for ATP hydrolysis and client activation. (4) Hsp90 repurposes one side of its client-binding sites to bind Hop_{DP2}, which in turn augments the Hsp90 lumenal client-binding site, facilitating client-loading from Hsp70 (Figs. 3b, 4a).

The loading complex provides an extremely extended client-binding pocket, with a large and very adaptable surface for client recognition (Figs. 3b, 4a, Extended Data Fig. 7b–d): (1) Hsp70 binds a hydrophobic strand; (2) Hop_{DP2} binds a hydrophobic or amphipathic helix; (3) the remaining part of the $Hsp90A_{amphi-\alpha}$ provides polar interactions; (4) the $Hsp90B_{amphi-\alpha}$ provides a hydrophobic surface; and (5) the Hsp90A/B lumen provides a combination of hydrophobic and polar interactions. Not only is the loading complex lumen spacious enough to bind a strand (as shown here) or intact helix (Extended Data Fig. 3f), but the flexible positioning of the $Hsp70C_{SBD}$ and the dynamic, adaptable conformation of the $Hsp90_{amphi-\alpha}$ allow even broader flexibility for client recognition.

Our structural insights reveal the molecular mechanism of GR inactivation in the chaperone cycle (Fig. 1a), allowing us to propose the following pathway for loading complex formation (Fig. 4b): Hsp70C captures the flexible $GR_{pre-Helix\,1}$, causing the next dynamic helix-strand motif to detach, thereby destabilizing the GR ligand-binding pocket (Extended Data Fig. 9b, c). Hsp70C then delivers the partially unfolded GR to Hop–Hsp70S–Hsp90. In the resultant loading complex, GR is further unfolded through engagement of the LXXLL motif of GR_{Helix1} with Hop_{DP2} and the $GR_{post-Helix1}$ strand with the Hsp90 lumen (Fig. 3b–d, Extended Data Fig. 8e), suppressing any possible ligand binding. The rest of GR remains globular and is only loosely associated with the distal surface of Hsp90.

Our structural data also enable us to propose how the loading complex progresses to the maturation complex–a process requiring Hsp90 ATP hydrolysis and release of Hop and both Hsp70s. The one-Hsp70 loading complex (Extended Data Fig. 3d, e) suggests that the process is asymmetric and sequential, with the loss of Hsp70C occurring first. Schematically shown in Fig. 4b, we propose that a combination of Hsp90's ATP binding and NEF activities promotes Hsp70C to hand off GR and exit the complex. This leaves GR engaged with Hop_{DP2} and the Hsp90 lumen, minimizing reformation of an Hsp70–GR complex or premature release. Then, asymmetric Hsp90 ATP hydrolysis drives the release of the more tightly engaged Hsp70S–Hop. Finally, as discussed in detail in a partner study[9], the conversion of the semi-closed Hsp90 in the loading complex to the fully closed $Hsp90^{ATP}$ in the maturation complex may serve as a driving force for client remodelling and hence activation (Extended Data Fig. 3b, c).

GR uses a generalized chaperone (Hsp70) and cochaperone (Hop) for loading onto Hsp90, making the principles learned here broadly applicable to other clients. Indeed, in this report, we show that the two most studied model clients–GR and v-Src–seemingly share a similar client-loading mechanism for their maturation (Extended Data Figs. 6j, 8h). Although Hop is absent in bacteria and organellar compartments, Hsp70s are ubiquitously present and the

client binding provided by Hop_{DP2} is probably substituted by the $Hsp90_{amphi-\alpha}$. Although most, if not all, proteins engage with Hsp70 at least during initial folding, only a subset are Hsp90 clients. Ultimately, client properties must dictate this selectivity. Rather than an overall client property such as stability, our loading complex structure suggests a more nuanced balance of three effects: (1) the probability of partial unfolding fluctuations in the client; (2) the ability of Hsp70 to capture a transiently exposed site; and (3) the likelihood that further unfolding events would uncover adjacent client regions that can be captured by Hop_{DP2}–Hsp90. Experiments to test these general principles can now be designed to predict and identify potential clients that undergo regulation by Hsp90 and Hsp70.

Methods

Protein purification

All recombinant chaperone proteins of Hsp90α, Hop and Hsp70 (from human), and ydj1 (yeast Hsp40) were in general expressed and purified as described previously[8] but with minor modifications as described below. Proteins were expressed in the *Escherichia coli* BL21 star (DE3) strain. Cells were grown in terrific broth (TB) at 37 °C until the optical density at 600 nm (OD_{600}) reached 0.8. Protein expression was induced with 0.5 mM IPTG for 16 h at 16 °C. Cells were collected by centrifugation at 4,000g for 15 min and resuspended in lysis buffer (50 mM Tris pH 7.5, 500 mM KCl, 10 mM imidazole and 5 mM βME). A protease inhibitor cocktail (Roche) was then added. Cells were lysed by an Emulsiflex system (Avestin). Lysates were cleared by centrifugation at 20,000 rpm for 1 h at 4°C and the soluble fraction was affinity-purified by gravity column with Ni-NTA affinity resin (Qiagen). The protein was eluted by 50 mM Tris pH 8, 50 mM KCl and 5 mM βME. The $6^{\times}$-His-tag was removed with TEV protease and protein was dialysed into low-salt buffer overnight (50 mM Tris pH 8, 50 mM KCl and 5 mM βME). The cleaved protein was purified with MonoQ 10/100 GL (GE Healthcare), an ion-exchange column with 30 mM Tris pH 8, 50 mM KCl and 5 mM βME and eluted with a linear gradient of 50–500 mM KCl. Fractions with the target protein were then pooled and concentrated for final purification of size exclusion in 30 mM HEPES pH 7.5, 50 mM KCl, 2 mM DTT and 10% glycerol using a Superdex S200 16/60 (GE Healthcare) or Superdex S75 16/60 (GE Healthcare). The peak fractions were pooled, concentrated to around 100–150 μM or greater, snap-frozen in liquid nitrogen and stored in aliquots at −80 °C. MBP–GRLBD(520–777) (F602S) was expressed and purified as described previously[8]. Note that for complex preparation, Hsp70 from an Sf9 cell source was used with purification as described previously[8]. The Hop and GR constructs for the cross-linking experiment were obtained using FastCloning[44] to the Amber codon. The constructs were expressed in *E. coli* BL21 DE3 cells containing the pEVOL-pBpF plasmid[45] distributed by the laboratory of P. Schultz through Addgene (31190). Cells were grown in TB to an OD_{600} of 0.6. For induction, arabinose (0.02%), IPTG (1 mM) and p-benzoyl-phenylalanine (pBpa; 0.7 mM) were added, and expression was carried out overnight at 16 °C. Cell collection, lysis and Ni-NTA purification was performed as described above.

Preparation of the GR-loading complex

Using reaction buffer containing 50 mM HEPES pH 7.5, 50 mM KCl and 2 mM DTT, 10 µM Hsp90 dimer of ATP-binding-deficient mutant (Hsp90(D93N))[46], 10 µM Hop, 15 µM Hsp70, 4 µM Hsp40 and 20 µM MBP-GRLBD were incubated with 5 mM ATP/MgCl$_2$ for 1 h at room temperature. The complex was purified and analysed by size-exclusion chromatography with multi-angle light scattering (SEC-MALS) with a Wyatt 050S5 column on an Ettan LC (GE Healthcare) in a running buffer containing 50 mM HEPES, 50 mM KCl, 5 mM MgCl$_2$, 2 mM DTT, 200 µM ADP and 0.01% octyl β-D-glucopyranoside (β-OG). Molecular weights were determined by multi-angle laser light scattering using an in-line DAWN HELEOS and Optilab rEX differential refractive index detector (Wyatt Technology Corporation). Once eluted, fractions containing the GR-loading complex were immediately cross-linked with 0.02% glutaraldehyde for 20 min at room temperature and quenched with 20 mM Tris pH 7.5. Fractions containing the GR-loading complex were separately snap-frozen in liquid nitrogen, and stored in aliquots at −80 °C.

Photoreactive cross-linking experiment

To ensure that pBpa-Hop (Extended Data Fig. 8a, b, d) and pBpa-GR (Extended Data Fig. 10) cross-link the bound segment in the context of the loading complex, cross-linking reactions were performed immediately after the complex was fractionated from SEC (see the previous section). Using a UV-transparent, 96-well microplate (Corning) as a fraction collector, the whole fractions of the eluted GR-loading complex were subjected to UV exposure using an agarose gel imaging system (Enduro GDS Imaging System). Samples were irradiated for 60 min in total. To prevent overheating, the 96-well plate was placed on a shallow, UV-transparent plate filled with constantly refreshed ice water during the time course of the exposure. SDS–PAGE gels were used to analyse cross-linked products, followed by western blot transfer to nitrocellulose and probed with anti-MBP (New England BioLabs), anti-Hsp70 (Enzo Life Sciences) or anti-STIP1 (Proteintech) antibodies.

Cryo-EM sample preparation, grid preparation and data acquisition

The flash-frozen fractions of the loading complex were thawed and concentrated to 0.7–0.8 µM. About 2.5 µl of the complex sample was applied onto a glow-discharged, holey carbon grid (Quantifoil R1.2/1.3, Cu,400 mesh), blotted by Vitrobot Mark IV (FEI) for 8–14 s at 10 °C and 100% humidity, and plunge-frozen in liquid ethane. Four data collections were made using Titan Krios (Thermo Fisher Scientific) equipped with a K2 camera (Gatan K2). SerialEM[47] was used for all the data collections with parameters as described in Supplementary Table 1.

Image processing

Movies were motion-corrected using MotionCor2[48], in which the unweighted summed images were used for CTF estimation using CTFFIND4[49], and the dose-weighted images were used for image analysis with RELION[50] throughout. The initial model of the loading complex was obtained from a small data collection (Extended Data Fig. 1d). Particles were picked from the small data collection using Gautomatch (https://www2.mrc-lmb.cam.ac.uk/research/locally-developed-software/zhang-software/) without template and

subjected to reference-free 2D classification (Class2d) using RELION. 2D class averages with proteinaceous features were selected for 3D classification (Class3d) using RELION. For Class3d, the reference model was generated using the semi-open conformation Hsp90 from the Hsp90–Hop cryo-EM structure[34] (Supplementary Fig. 7c). Among eight classes, one class (around 8 Å resolution) showed recognizable shapes of the protein components, although the class is markedly different from the initial model (Extended Data Fig. 1d). This low-resolution reconstruction of the loading complex was then used as an initial reference model for the following image analysis that achieved high resolution.

The procedure to obtain the high-resolution reconstruction is shown schematically in Extended Data Fig. 1e. Particles were picked from all dose-weighted micrographs using Gautomatch with the low-resolution reconstruction as a template. Without using Class2d, the extracted, binned 4×4 particles (4.236 Å pixel^{-1}) were subjected to RELION Class3d (4 classes) to sort out 'empty' or non-proteinaceous particles. Particles from the selected class were re-centred and re-extracted to binned 2×2 (2.118 Å pixel^{-1}) for another round of Class3d. Note that a low-resolution (around 7.5 Å) reconstruction of one-Hsp70 loading complex was obtained among the 4 classes (Extended Data Fig. 1e). The selected class that contains 636,056 particles of the two-Hsp70 loading complex was 3D auto-refined (Refine3d) into a single class (consensus class). The set of particles are then used for further global classification and focused classification (described below). For global classification, another round of masked Class3d (4 classes) was performed without alignment, followed by masked Refine3d using unbinned particles (1.059 Å pixel^{-1}). Finally, 85,619 particles from the highest resolution, two-Hsp70 loading class were further subjected to multiple rounds of per-particle CTF and beam-tilt refinement[51] until the gold-standard resolution determined by Refine3d no longer improved. The overall gold-standard resolution for the global reconstruction of the loading complex is 3.57 Å (Extended Data Fig. 2c). Local resolution was estimated using RELION (Extended Data Fig. 2a).

The loading complex presents conformational heterogeneity at all regions of the complex, in particular at the Hop$_{TPR2A-TPR2B}$ (Supplementary Fig. 5f–h). Starting from the consensus class containing 636,056 binned 2×2 particles (2.118 Å pixel^{-1}), masks at various GR-loading complex regions were used for focused classification with signal subtraction using RELION[52] (Focused-class3d) (Extended Data Figs. 1f, 2g). A pipeline to obtain the best reconstruction for each masked region is outlined in Extended Data Fig. 1f. For each masked region, Class3d without alignment was performed, followed by Refine3d using unbinned particles (1.059 Å pixel^{-1}). For each Class3d job, parameters of number of requested classes ($K = 6, 8, 10, 12, 14$) and Tau ($T = 10, 20, 30, 40$) were scanned. For each masked region, the reconstruction that results in the highest resolution determined by the gold-standard Fourier shell correlation (FSC) of the Refine3d job was selected for each masked region. Using the unbinned particles, another round of Focused-class3d was performed with the similar procedure described for the previous round. Parameters were scanned in a similar manner but with smaller requested classes ($K = 2, 3, 4, 5$). Finally, the selected Focused-class3d job was subjected to multiple rounds of per-particle CTF and beam-tilt refinement. The overall resolution of the reconstruction for each masked region is determined by the gold-standard FSC and as denoted in the FSC plots in Extended Data Fig.

2g, Supplementary Table 2. The focused maps showed much better atomic details than the global reconstruction at all regions, and hence were used for model building and refinement.

Model building and refinement

Model building and refinement was carried out using Rosetta[53] throughout. All of the components of the loading complex had crystal structures or close homologous structures (from yeast) available. Details of how the starting, unrefined atomic model for each component was obtained are described below. For Hsp90, the starting model was assembled from the crystal structure of human apo-Hsp90$_{NTD}$ (PDB ID: 3T0H)[54] and the cryo-EM structure of the Hsp90$_{MD-CTD}$ from the GR-maturation complex[9]. Many crystal structures of Hsp70$_{NBD}$ were available. As potassium and magnesium ions were used in the buffer for complex preparation and there is density accounted for them in our focused maps (Supplementary Fig. 3a, b), the ADP state Hsp70$_{NBD}$ crystal structure (PDB ID: 3AY9)[55], which has potassium and magnesium ions to coordinate ADP, was used as an starting model. For the Hsp70$_{SBD-\beta}$, the human Hsp70 crystal structure (PDB ID: 4PO2)[56] was used as a starting model. The initial docking poses of Hsp70C$_{SBD-\beta}$ were obtained using a rotation search enabled by spherical-harmonic decomposition previously used[57] for docking fragments in cryo-EM density. To facilitate the rotation search, the density of Hsp70C$_{SBD-\beta}$ was isolated from the 5A low-pass-filtered map of the global reconstruction using the Chimera "Zone" tool. The top solution was selected from the top-10 solutions based on (1) visual inspection of the fit-to-density, (2) the physical connectivity to the C-terminus of Hsp70C$_{NBD}$, (3) the room to accommodate the Hsp70C$_{SBD-\alpha}$ (shown as missing density in the global reconstruction), and (4) the cryo-EM density and physical connectivity of the bound GR segment in Hsp70C$_{SBD-\beta}$ to the GR segment in the lumen of the loading complex. The interdomain linker between Hsp70C$_{NBD}$ and Hsp70C$_{SBD-\beta}$ was built using RosettaCM guided by the 5 Å low-pass-filtered map of the global reconstruction with all of the complex components present. Then, the docking pose of Hsp70C$_{SBD-\beta}$ was further optimized with full-atom energy minimization guided by the cryo-EM density. The sequence of the Hsp70C$_{SBD-\beta}$-bound GR segment was determined with the aid of Rosetta (Supplementary Fig. 9). Two 7-residue GR segments (SIVPATL and IVPATLP) of a continuous sequence (residues 519–526; note that residue 519 in the native GR sequence is T, not S) in the GR$_{pre-Helix\ 1}$ strand are predicted to be Hsp70-binding sites by two state-of-the-art algorithms (BiPPred[58] and ChaperISM[59]) (Extended Data Fig. 9a). Structural modelling of the two GR peptides in the templates[60] (PDB IDs: 4EZZ, 4EZT and 4EZQ) with 'reverse' binding mode to Hsp70C$_{SBD-\beta}$ indicated that the segment, SIVPATL, is energetically more favoured (Supplementary Fig. 9a–c). For Hop, the crystal structures[33] of the Hop$_{TPR2A-TPR2B}$ (PDB ID: 3UQ3) and Hop$_{DP2}$ (PDB ID: 2LLW) from yeast were used as initial templates with the alignments obtained from the HHpred server[61] (Supplementary Fig. 5a, b, e). The insertion in the threaded Hop model was completed using RosettaCM[62] guided by the cryo-EM density. The resulting completed models of Hop$_{TPR2A}$ and Hop$_{TPR2B}$ showed a high resemblance to their structures determined by NMR[63] individually (Supplementary Fig. 5c, d).

Using the high-resolution information acquired from focused classification/refinement, the starting models were refined separately into the individual focused maps (Extended Data

Fig. 2g). Model overfitting was monitored and contained using the half-map approach as previously described[64,65], in which one-half map from RELION Refine3d was used for density-guided refinement, whereas the other half map was used for validation. A Rosetta fragment-based iterative refinement protocol[65] was used to refine the models throughout. On the basis of the high-resolution focused maps, the refinement tasks were split into (1) Hsp90A–Hsp70C (Extended Data Fig. 2g, Supplementary Fig. 1a), (2) Hsp90B–Hsp70S (Extended Data Fig. 2g, Supplementary Fig. 1b), (3) Hsp70S–Hop$_{TPR2A}$ (Extended Data Figs. 2g, 6a, d) and (4) Hsp90AB$_{CTD}$–Hsp70S$_{SBD-\beta}$–Hop$_{DP2}$–GR$_{Helix\ 1}$ (Extended Data Figs. 2g, 7a–c). To model the GR segment threaded through the lumen of Hsp90, the GR$_{Helix\ 1}$ motif (residues 528–551) was first segmented from the crystal structure of GR$_{LBD}$ (PDB ID: 1M2Z)[66] and rigid-body-fitted into the lumen density. The GR$_{Helix1}$ segment was then rebuilt and refined using a Rosetta fragment-based iterative refinement method into the focused map of the Hsp90AB$_{CTD}$–Hsp70S$_{SBD-\beta}$–Hop$_{DP2}$–GR$_{Helix\ 1}$ (Extended Data Figs. 2g, 7a–c) with the other component proteins present. The remaining, globular portion of GR$_{LBD}$ was rigid-body-fitted initially using Chimera. The placement was further refined, guided by (1) the connectivity to the GR$_{Helix1}$ motif and (2) GR's interaction with Hsp90$_{MD}$ in the maturation complex[9]. The docked GR$_{LBD}$ was then energy minimized in Rosetta guided by the 10 A low-pass-filtered cryo-EM map (Extended Data Fig. 7f, g). Finally, the connectivity of the N-terminal end of the globular portion of GR$_{LBD}$ and the C-terminal end of the GR$_{Helix1}$, and the N-terminal end of the GR$_{Helix1}$ motif and the C-terminal end of the Hsp70-bound GR$_{pre-Helix\ 1}$ portion (Supplementary Fig. 9d–f), was built using RosettaCM. Note that the N-terminal MBP (maltose-binding protein) tag of the GR$_{LBD}$ construct was ruled out to be the density connected to the GR$_{pre-Helix\ 1}$ (Supplementary Fig. 8c). The final model of the loading complex was assembled and refined into the high-resolution global construction, followed by atomic *B*-factor refinement (Extended Data Fig. 2d–f). Note that the dynamic range of the fitted atomic *B*-factors (Extended Data Fig. 2d, e) accurately represents the distribution of local-resolution estimates in the global reconstruction shown in Extended Data Fig. 2a.

Structural modelling was used to ensure and suggest the connectivity of the EEVD tails of Hsp90–Hsp70 to the bound TPR domains of Hop (Supplementary Fig. 7a, b). For each protomer of Hsp90, around 40 residues of the tail were modelled using RosettaCM to connect the bound Hsp90 EEVD fragment and the very C-terminal helix in the Hsp90$_{CTD}$. Similarly, for Hsp70C, the remaining residues were built, including a Hsp70$_{SBD-\alpha}$ lid closing on the Hsp70$_{SBD-\beta}$ (PDB ID: 4PO2)[56] followed by approximately 30-residue tail residues to the Hsp70 EEVD fragment bound to Hop$_{TPR2B}$.

To investigate how the NEFs, Bag-1[30] and Hsp110[31,67], may regulate the GR cycle using the canonical NEF-binding site on the Hsp70$_{NBD-IIB}$ in the loading complex, crystal structures of the Hsc70$_{NBD}$–Bag-1 complex (PDB ID: 1HX1)[68] and Hsp70$_{NBD}$–yeast Hsp110 complex (PDB ID: 3D2E)[69] were superimposed onto the Hsp70s in the loading complex using PyMOL.

In vivo yeast Hsp90–Hsp70 interaction assay

Hsc82 plasmids expressing untagged or His–Hsc82 were expressed in the yeast strain JJ816 (*hsc82::LEU2 hsp82::LEU2/YEp24-HSP82*). His–Hsc82 complexes were isolated as described[70]. Antibodies against the last 56 amino acids of Ssa1/2 were a gift from E. Craig. The Sti1 peptide antiserum was raised against amino acids 91–108. His–Hsc82 was detected using an anti-Xpress antibody, which recognizes sequences near the 6×-His tag at the amino terminus. The R46G and K394E mutations were isolated in a genetic screen as described[23].

Expression of Sti1 mutants

Wild-type cells (JJ762), or *sti1* cells (JJ623) expressing empty vector (pRS315) or plasmid-borne wild-type or mutant Sti1 (pRS315-*STI1*) were lysed and subjected to SDS–PAGE (7.5% acrylamide gel) followed by immunoblot analysis with polyclonal antisera raised against yeast Sti1 as previously described[71].

Growth assay of STI1 function

hsc82hsp82 (*hsc82hsp82/YEp24-HSP82*) (JJ117) or *sti1hsc82hsp82/YEp24-HSP82* (JJ1443) strains were first transformed with plasmids expressing wild-type *HSC82* or *hsc82-G309S* (pRS313GPDHis-Hsc82). Those cells were transformed with an additional plasmid, either empty vector (pRS315), or wild-type or mutant Sti1 (pRS315-*STI1*). Transformants were grown for 3 days in the presence of 5-FOA, which counter-selects for the URA3-based YEp24-*HSP82* plasmid. As previously shown[23], *sti1hsc82hsp82* cells expressing *hsc82-G309S* are viable in the presence of *STI1* but inviable in *sti1* cells. Viability of *sti1hsc82hsp82* cells expressing *hsc82-G309S* is restored by the presence of a plasmid expressing wild-type *STI1* but not mutant *sti1*.

v-Src assay

Wild-type cells (JJ762), or *sti1* cells (JJ623) expressing empty vector (pRS315), or plasmid-borne wild-type or mutant Sti1 (pRS315-*STI1*) were transformed with a plasmid expressing v-Src (pBv-src) under the *GAL1* promoter or a control plasmid (pB656)[71].

Cells were grown overnight in raffinose medium lacking uracil. The next day, galactose was added to a final concentration of 2%. After six hours of incubation, the cells were serially diluted 10-fold, spotted on the indicated media and grown for 2 days (glucose) or 3 days (galactose). All strains exhibited similar growth in the presence of glucose. v-Src induction in the presence of galactose dramatically inhibited the growth of wild-type but not *sti1* cells. Adding plasmid borne *STI1* resulted in growth inhibition, similar to wild-type cells. Cells expressing mutant forms of *STI1* behaved like cells expressing empty vector.

Reporting summary

Further information on research design is available in the Nature Research Reporting Summary linked to this paper.
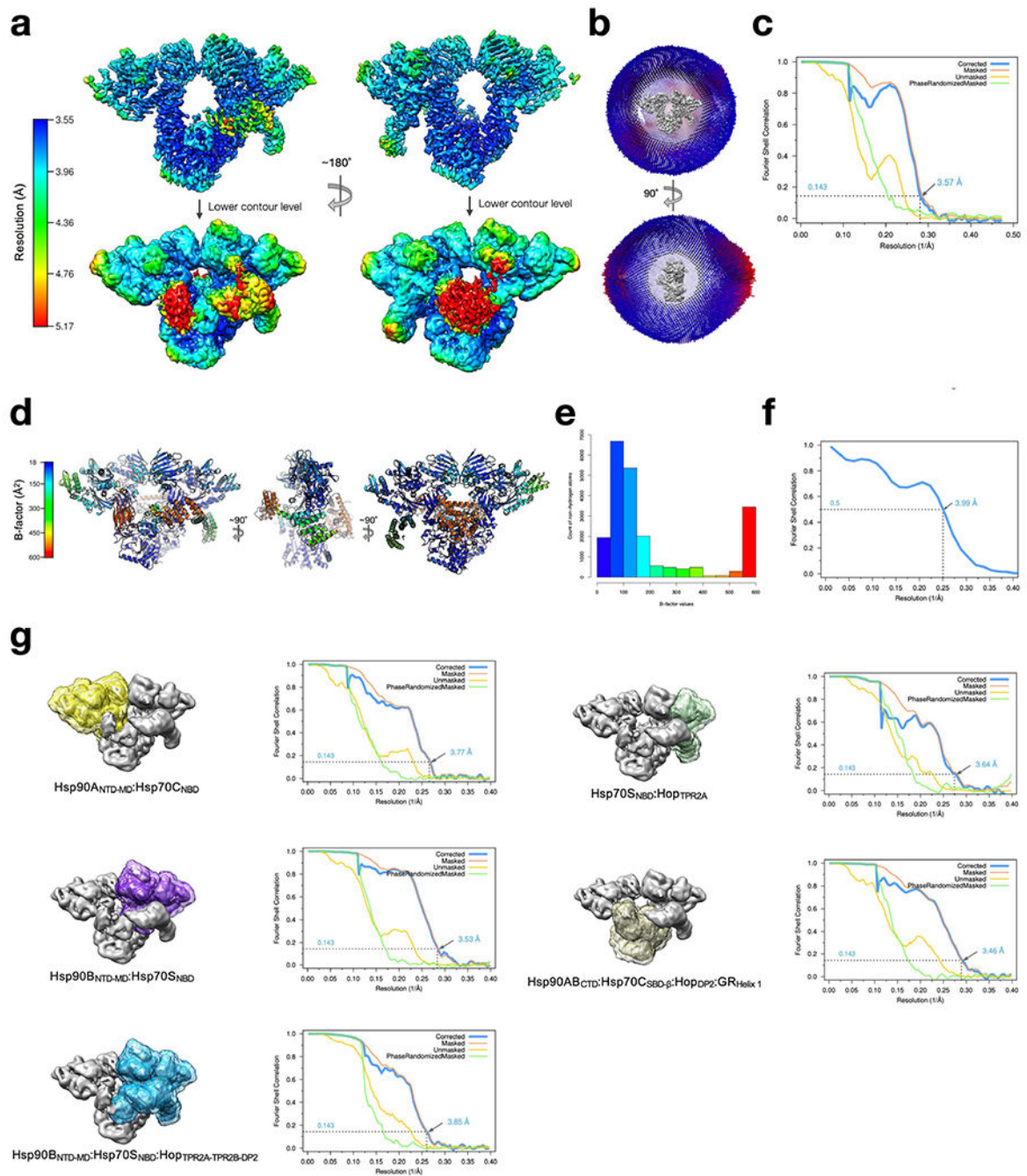
Extended Data
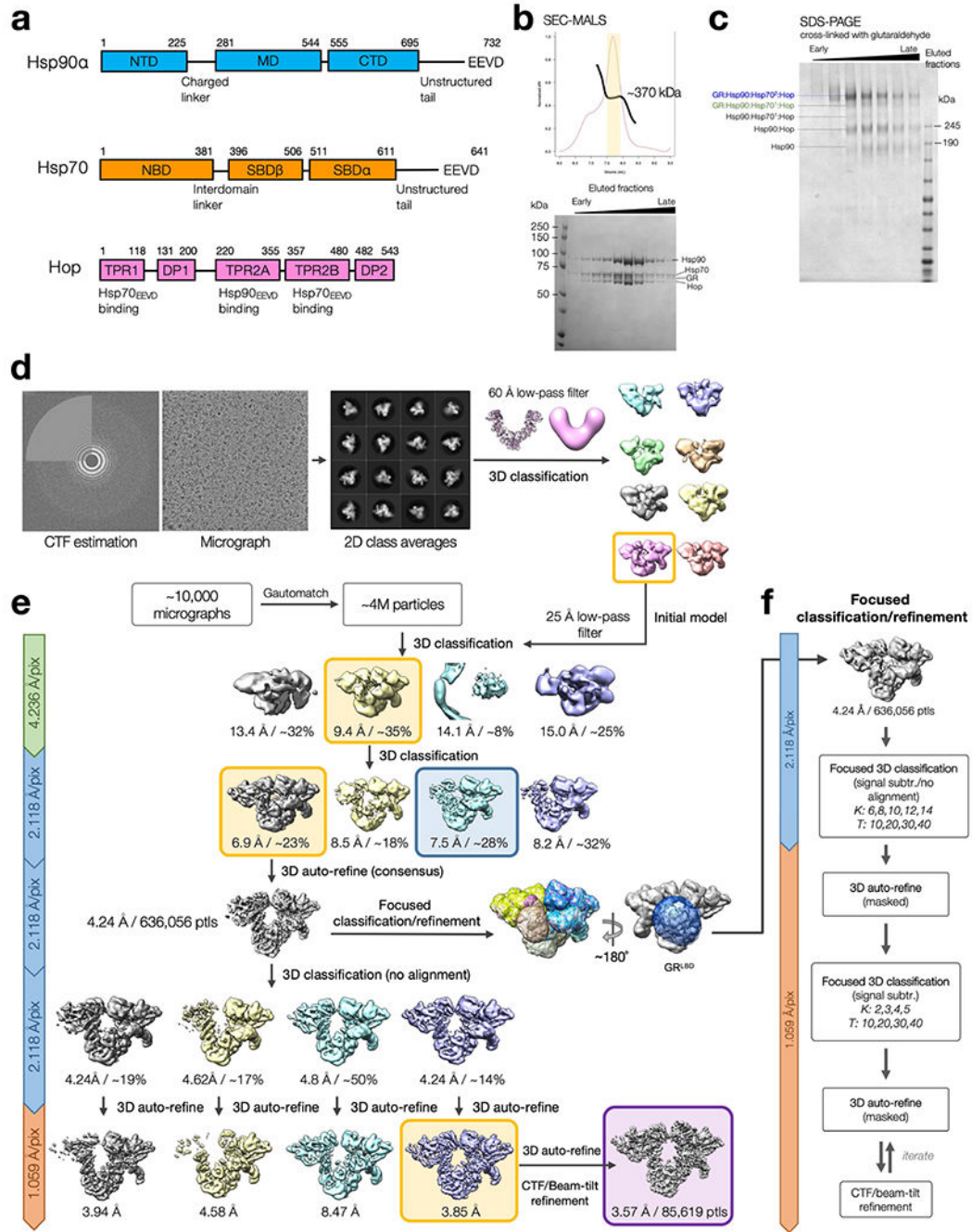
Extended Data Fig. 1 |. Purification of the GR-loading complex and the cryo-EM single-particle image processing pipeline.

a, Domain organization of the chaperone proteins in the GR-loading complex. **b**, Top, elution profile of gel filtration using SEC-MALS to confirm the homogeneity of the GR-loading complex. The apparent molecular weight of the eluent estimated by SEC-MALS is ~370 kDa, although the two-Hsp70 client-loading complex is ~440 kDa. The discrepancy may be a result of multiple species co-eluted. Bottom, SDS–PAGE stained with Coomassie

blue of the eluted fractions marked in (top). **c**, SDS–PAGE stained with Coomassie blue of the fractions treated with 0.02% (w/v) glutaraldehyde cross-linking for 20 min at room temperature, followed by quenching with 20 mM Tris buffer at pH 7.5. Data in (**b-c**) are representative data of at least two independent experiments. **d**, Initial model generation for the GR-loading complex. The 60 Å low-pass filtered initial model used to reconstruct the 3D model was adopted from the Hsp90 semi-open conformation structure from the Hsp90:Hop cryo-EM structure[34]. **e**, Schematic workflow of the global cryo-EM map reconstruction. Yellow boxes indicate the selected class to move forward. Blue box indicates one-Hsp70 loading complex. Purple box indicates the final high-resolution global reconstruction. **f**, Flow chart of focused classification/refinement using the signal subtraction approach from RELION. Final reconstructions for individual masked classifications/refinements were selected based on the resolution intercepted with the FSC 0.143 from 3D auto-refine. K=number of classes; T=regularization factor, Tau.

Extended Data Fig. 2 |. Resolution estimates for cryo-EM reconstructions, atomic B-factor refinement and model-map FSC.

a, Local resolution estimates for the GR-loading complex global reconstruction were calculated using RELION with front view (left) and back view (right). **b**, Euler angle distribution in the final reconstruction. Orthogonal views of the reconstruction are shown with front view (top) and side view (bottom) **c**, Gold-standard FSC for the global cryo-EM reconstruction. **d**, Atomic model with B-factors refined with colour key shown on the left. **e**, Histogram of the B-factor values of all non-hydrogen atoms in the atomic model, coloured

by the same colour key in **d**. **f**, Model-map FSC. **g**, Focused classification and refinement of the GR-loading complex. Masks were created at various regions of the GR-loading complex (left) and its corresponding gold-standard FSC (right) after 3D auto-refine. The nominal resolution for each reconstruction is labelled and indicated in the FSC plots.
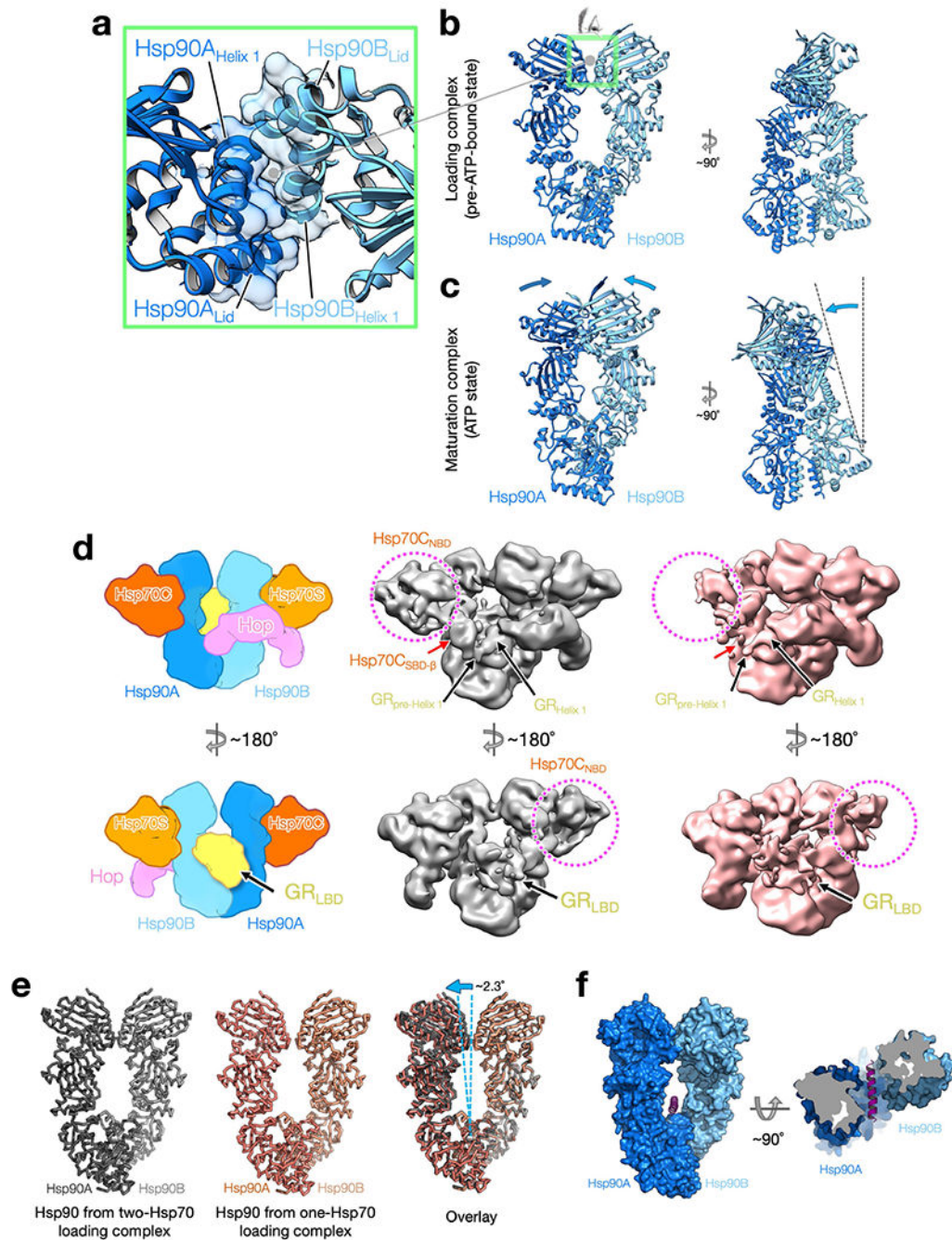
Extended Data Fig. 3 |. The Hsp90 in both two-Hsp70 and one-Hsp70 GR-loading complexes adopts a semi-closed conformation.

a, Close-up view of the novel dimerization interface of the symmetric Hsp90 dimer with residues at the interface in transparent surface representation. The interface is composed

of two molecular switches of Hsp90, the first helix and the lid motif. **b**, **c**, The Hsp90 in the loading complex (**b**) is one step away from the fully closed ATP state (**c**). Front (left) and side (right) views of the Hsp90 in the two-Hsp90 GR-loading complex (**b**) and the Hsp90 in the GR-maturation complex[9] (**c**). Arrows indicate displacements from the Hsp90 in the loading state, in which a large twisting motion is apparent from the side view. **d**, Comparison of cryo-EM reconstructions of the one-Hsp70 and two-Hsp70 GR-loading complexes. Schematic model of the two-Hsp70 loading complex (left). Front views of cryo-EM maps of the two-Hsp70 (middle; grey colour) and one-Hsp70 (right; salmon colour) GR-loading complexes. Right, the one-Hsp70 reconstruction has lost density for $Hsp70C_{NBD}$ (dashed circle) and $Hsp70C_{SBD\text{-}\alpha}$ (red arrows); however, density for $GR_{pre\text{-}Helix\ 1}$ and $GR_{Helix\ 1}$ (black arrows) is in the same location as it is in the two-Hsp70 GR-loading complex. **e**, Rigid-body fitting of the two Hsp90 protomers individually in the one-or two-Hsp70 loading complexes cryo-EM reconstructions shows both of the Hsp90s share a similar semi-closed conformation. The Hsp90 in the one-Hsp70 loading complex (middle panel) has a slightly wider opening angle (right panel) than the Hsp90 in the two-Hsp70 loading complex (left panel). **f**, The lumen of the semi-closed Hsp90 presented in the loading complex can fit a helix[72]. A helix (magenta) can be accommodated in the semi-closed Hsp90. Front view (left) and top view (right).
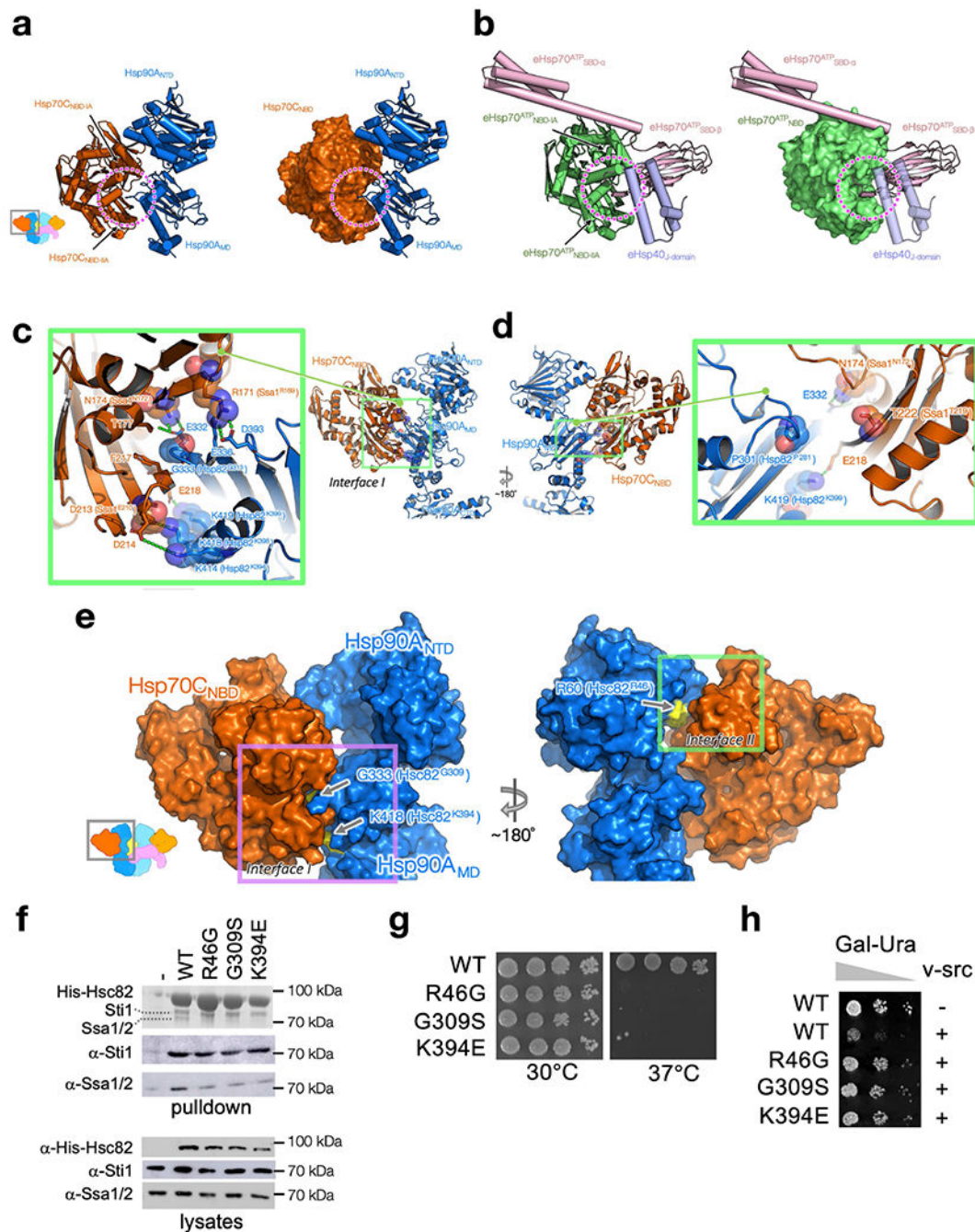
Extended Data Fig. 4 |. Interfaces I and II are both crucial for Hsp90–Hsp70 interactions and client activation.

a, **b**, The Hsp70 cleft (dashed circles), formed by $Hsp70_{NBD-IA}$ and $Hsp70_{NBD-IIA}$ (**a**), which $Hsp90_{MD}$ interacts with, is used by the Hsp70 interdomain linker in the $Hsp70^{ATP}$ state and Hsp40's J-domain (**b**). Hsp90A:Hsp70C in the loading complex are shown as cartoon (**a**, left) and surface (**a**, right) representation. The *E. coli* Hsp70 (eHsp70):J-protein complex in the ATP state (PDB ID: 5NRO[73]) are shown as cartoon (**b**, left) and surface (**b**, right) representation. The two subdomains of eHsp70 are

coloured in green for $eHsp70^{ATP}_{NBD}$ and in pink for $eHsp70^{ATP}_{SBD}$. The *E.coli* Hsp40 J-domain ($eHsp40_{J-domain}$) is coloured in purple. **c, d**, Mapping Hsp90/Hsp70 residues previously characterized by the Wickner group on the loading complex. Five yeast Hsp90 ($Hsp82^{P281,G313,K394,K398,K399}$)[23] and four yeast Hsp70 ($ssa1^{R169,N172,E210,T219}$)[24] mutations previously characterized by the Wickner group[23,24] are all located at Interface I. These 'Wickner residues' are shown with stick and transparent sphere representation, whereas residues that interact with the Wickner residues are shown with only stick representation. Polar interactions are highlighted with green dashed lines. Residue numbers of the Wickner residues in yeast Hsp90/Hsp70 are shown as the labels within parentheses. Based on the proximity of the Wickner residue positions to Interface I residues, our structure can readily explain why $Hsp82^{P281C\ (P301,\ Hsp90)}$ and $Ssa1^{T219C(T222,\ Hsp70)}$ (**d**) showed no effect, whereas the other four Hsp90 mutants ($Hsp82^{G313S(G333,\ Hsp90)}$, $Hsp82^{K394C(K414,Hsp90)}$, $Hsp82^{K398E(K418,Hsp90)}$, $Hsp82^{K399C(K419,\ Hsp90)}$) and the other three Hsp70 mutants ($Ssa1^{N172D(N174,\ Hsp70)}$, $Ssa1^{R169H(R171,\ Hsp70)}$, $Ssa1^{E210R(D213,\ Hsp70)}$) (**c**) disrupted Hsp90:Hsp70 interaction significantly. **e–h**, In vivo validation of Interface I and II of the Hsp90:Hsp70 interactions in the GR-loading complex. Mapping the positions of the three mutations (arrows and yellow surface representation in **e**) used for in vivo validation on the atomic structure of Hsp90:Hsp70 (dark blue:dark orange; surface representation in **e**) in the GR-loading complex. The Interface I residues used, $Hsp90^{G333}$ ($Hsc82^{G309}$) and $Hsp90^{K418}$ ($Hsc82^{K394}$), are indicated by arrows (**e**, left panel). The Interface II residue, $Hsp90^{R60}$ ($Hsc82^{R46}$), is indicated by an arrow (**e**, right panel). Residue numbers of the residues in yeast Hsc82 are shown as the labels within parentheses in **e**. In **f**, His-Hsc82 complexes were isolated from yeast and analysed by SDS-PAGE and visualized by Coomassie staining and immunoblot analysis (see also Supplementary Fig. 10 for the uncropped gels/blots). Yeast proteins: Sti1=Hop; Ssa1/2=Hsp70; Hsc82=Hsp90β. In **g**, plasmids expressing wild-type or mutant Hsc82 were expressed as the sole Hsp90 in JJ816 (*hsc82hsp82*) cells. Growth was examined by spotting 10-fold serial dilutions of yeast cultures on rich media, followed by incubation for two days at 30 °C or 37°C. In **h**, strains expressing wild-type (WT) or mutant *HSC82* were transformed with a multicopy plasmid expressing *GAL1*-v-src (pBv-src) or the control plasmid (pB656)[74]. Yeast cultures were grown overnight at 30 °C in raffinose-uracil drop-out medium until mid-log phase. Galactose (20%) was added to a final concentration of 2%. After six hours, cultures were serially diluted 10-fold onto uracil drop-out plates containing galactose. Plates were grown for 2-3 days at 30°C.
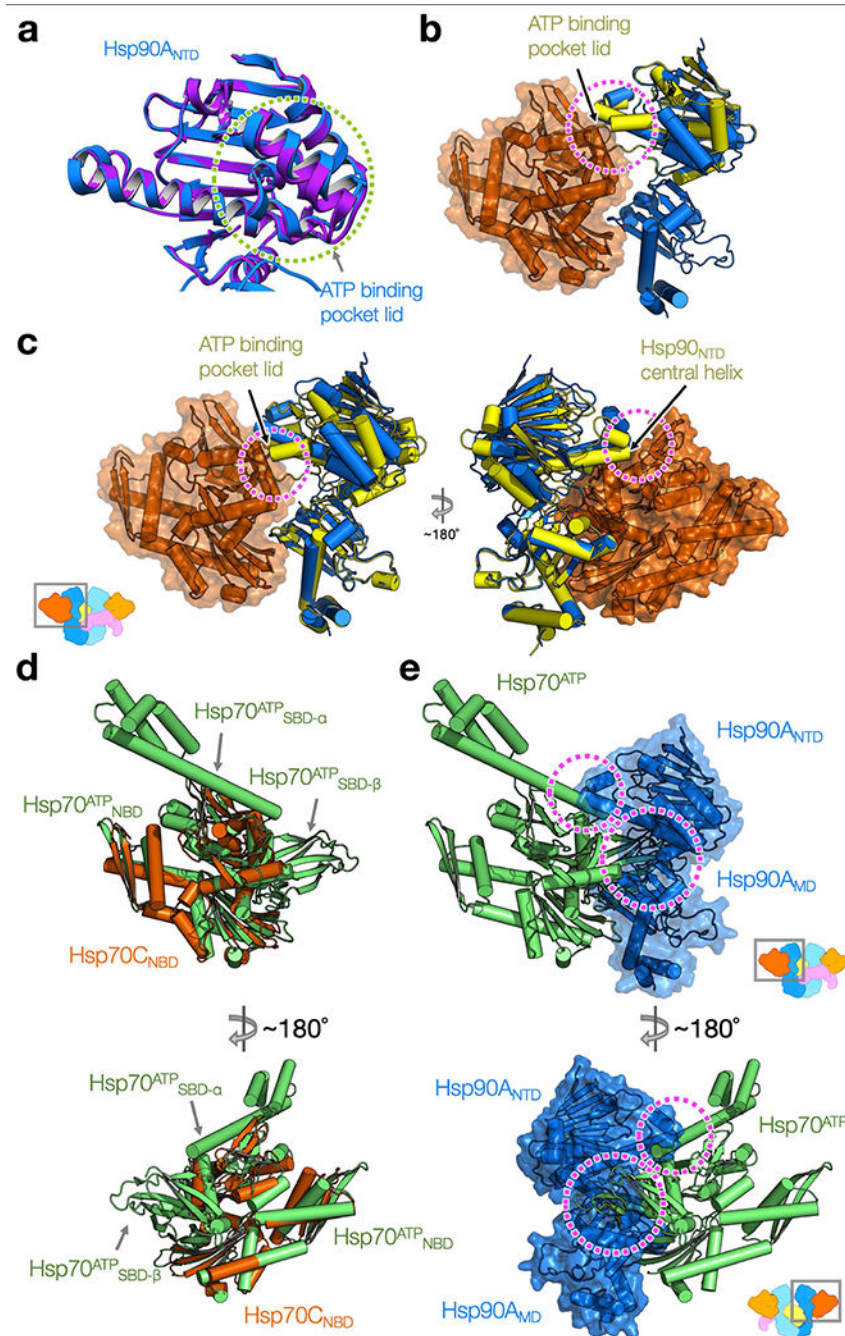
Extended Data Fig. 5 |. Both the Hsp90^{ATP} and the Hsp70^{ATP} conformations are incompatible with the GR-loading complex.

a, Overlay of the crystal structure of Apo Hsp90 fragment (purple; PDB ID: 3T0H[54]) to the Hsp90A$_{NTD}$ (dark blue). Green circle highlights the open ATP pocket lid. **b**, Closure of the ATP pocket lid in the ATP state of Hsp90$_{NTD}$ (the Hsp90α structure from the GR-maturation complex[9] is in yellow, ribbon representation) clashes (magenta circle) with the Hsp70$_{NBD}$ (orange, surface and ribbon representation) in the loading complex. The NTD fragment of Hsp90^{ATP} is aligned with the Hsp90$_{NTD}$ in the loading complex. **c**,

Superimposition of the ATP state of $Hsp90_{NTD-MD}$ fragment (yellow) to the Hsp90A (dark blue) at the MD. Magenta circles indicate steric clashes of the ATP state of the $Hsp90_{NTD}$ to the $Hsp70_{NBD}$ (orange; surface/ribbon representation). **d**, Superposition of the $Hsp70^{ATP}$ conformation (green; PDB ID: 4B9Q[75]) to the $Hsp70C_{NBD}$ (dark orange). Arrows indicate the two subdomains of $Hsp70^{ATP}_{SBD}$, which cause serious steric clashes with the Hsp90 in the loading complex shown in **e**. **e**, The superimposed $Hsp70^{ATP}$ shown in **e** is fixed from **d** and the Hsp90 (dark blue; surface/ribbon representation) of the GR-loading complex is present. Magenta circles highlight steric clashes caused by the two subdomains of $Hsp70^{ATP}_{SBD}$ (green) to the $Hsp90A_{NTD-MD}$.
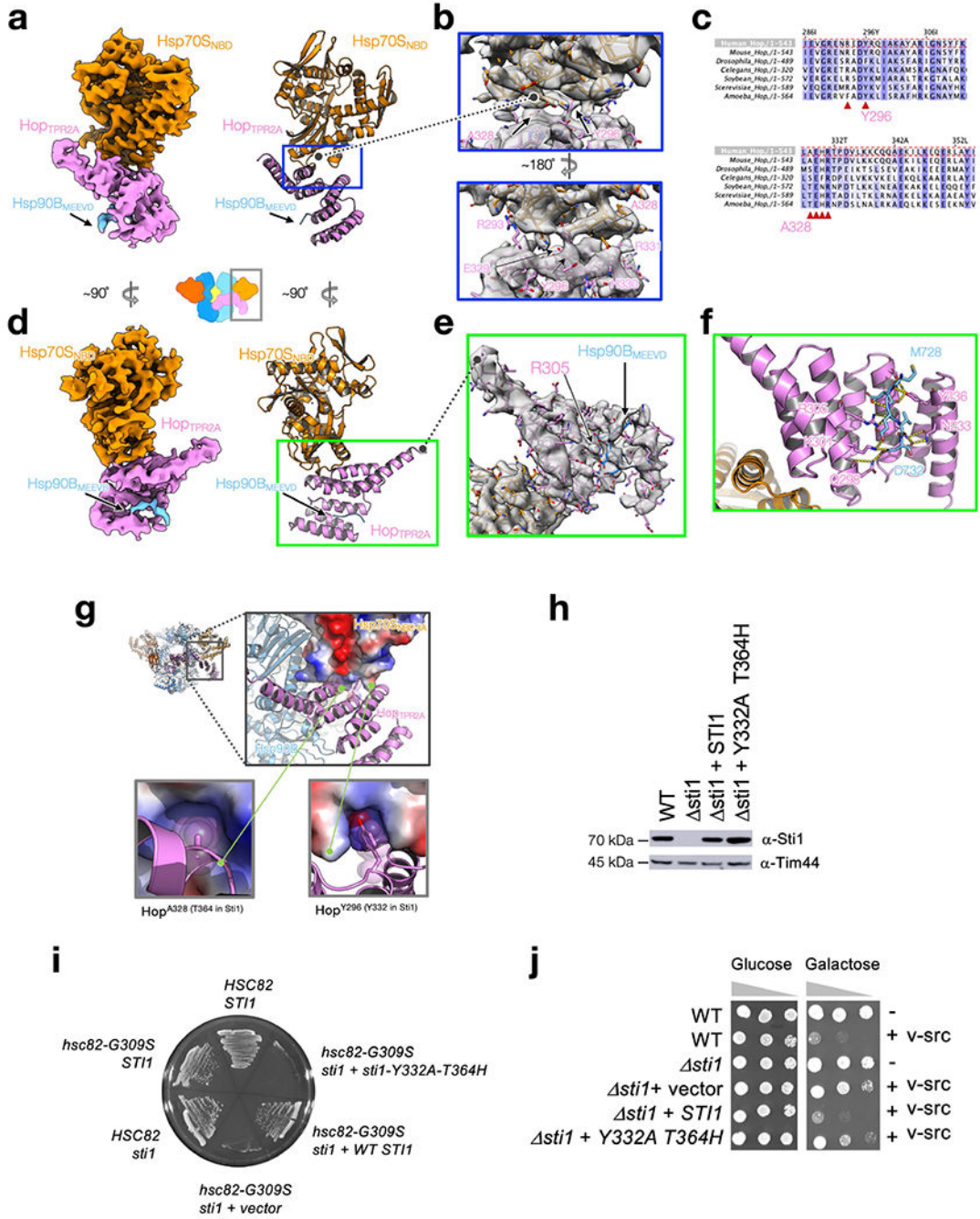
Extended Data Fig. 6 |. The Hsp70–Hop interface in the GR-loading complex is crucial for cellular functions and client maturation.

a–f, The atomic interactions of Hsp70S$_{NBD}$:Hop$_{TRP2A}$:Hsp9GB$_{MEEVD}$ in the GR-loading complex. The cryo-EM map from focused classification and refinement is shown in (**a** and **d**, left). The atomic model with the corresponding view from (**a** and **d**, left) is shown in the right panels of (**a**, **d**). Close-up views of the Hsp70S$_{NTD}$:Hop$_{TPR2A}$ interface with the atomic model fit into the density (**b**). Two key residues (Hop^{Y296} and Hop^{A328}) are buried in the surface with their sidechain density indicated by the arrows (**b**, top and bottom). Density of

the interface residues highlighted in Fig. 2b is shown in (**b**, bottom). Sequence alignments of Hop with key residues at the $Hsp70_{NBD}:Hop_{TPR2A}$ interface highlighted by the red triangles in (**c**), in which the colour scheme is BLOSUM62. Close-up view of the atomic model of $Hop_{TPR2A}:Hsp90B_{MEEVD}$ fit with the cryo-EM map is shown in (**e**). Close-up view of the atomic interactions of the MEEVD fragment from Hsp90B (light blue) and Hop_{TPR2A} (pink) from **e** is shown in **f**, in which polar interactions are depicted with dashed lines. **g**–**j**, In vivo validation of the $Hsp70S_{NBD}:Hop_{TPR2A}$ interface in the loading complex. The two buried residues in $Hsp70S_{NBD-IIA}:Hop_{TPR2A}$ interface, which were chosen for the mutational studies, are shown in **g**. Components of the GR-loading complex (**g**, top left) are coloured as in other figures and as labelled. $Hsp70S_{NBD}$ is shown in surface-charge representation (blue: positive; red: negative) calculated using PyMOL. Note that the corresponding residue numbering of the two positions in yeast Hop (Sti1) are shown in parentheses of the labels of the bottom panels in **g**. In **h**, $Sti1^{Y332A-T364H}$ accumulates at levels similar to WT Sti1 (see also Supplementary Fig. 10 for the uncropped gels/blots); data in **h** are representative of two independent experiments. Extracts from WT cells (JJ762), *sti1* cells (JJ623), or *sti1* cells transformed with a plasmid that expresses WT Sti1 or $Sti1^{Y332A-T364H}$ were analysed by SDS–PAGE and immunoblotted with a polyclonal antisera specific for Sti1. Loading control is antibody against mitochondrial protein Tim44. In **i**, *sti1-Y332A-T364H* is inviable in *hsc82hsp82* cells expressing *hsc82-G309S*. *hsc82hsp82* (JJ117) or *sti1hsc82hsp82* (JJ1443) strains harbouring YEp24-HSP82 were transformed with plasmids expressing WT *HSC82* or *hsc82-G309S*. Strains that lacked *STI1* were also transformed with an empty plasmid or a plasmid expressing WT *STI1* or *sti1-Y332A-T364H*. Transformants were grown in the presence of 5-FOA for 3 days to counter-select for the *YEp24-HSP82* plasmid. *STI1* is essential under these conditions and the growth of cells expressing *sti1-Y332A-T364H* was indistinguishable from those expressing the empty plasmid. In **j**, WT cells, *sti1* cells or *sti1* cells transformed with a plasmid that expresses WT Sti1 or Sti1-Y332A-T364H were transformed with an empty plasmid or a plasmid that expresses GAL-v-src. v-src induction in the presence of galactose sharply reduces the growth of WT cells, but not cells lacking *STI1*. The growth of cells expressing *sti1-Y332A-T364H* was very similar to those expressing the empty plasmid, indicating that *sti1-Y332A-T364H* is unable to support v-src function. The growth of cells in the presence of glucose was indistinguishable. 10-fold serial dilutions of cultures were grown for 3 days in the presence of galactose or glucose.
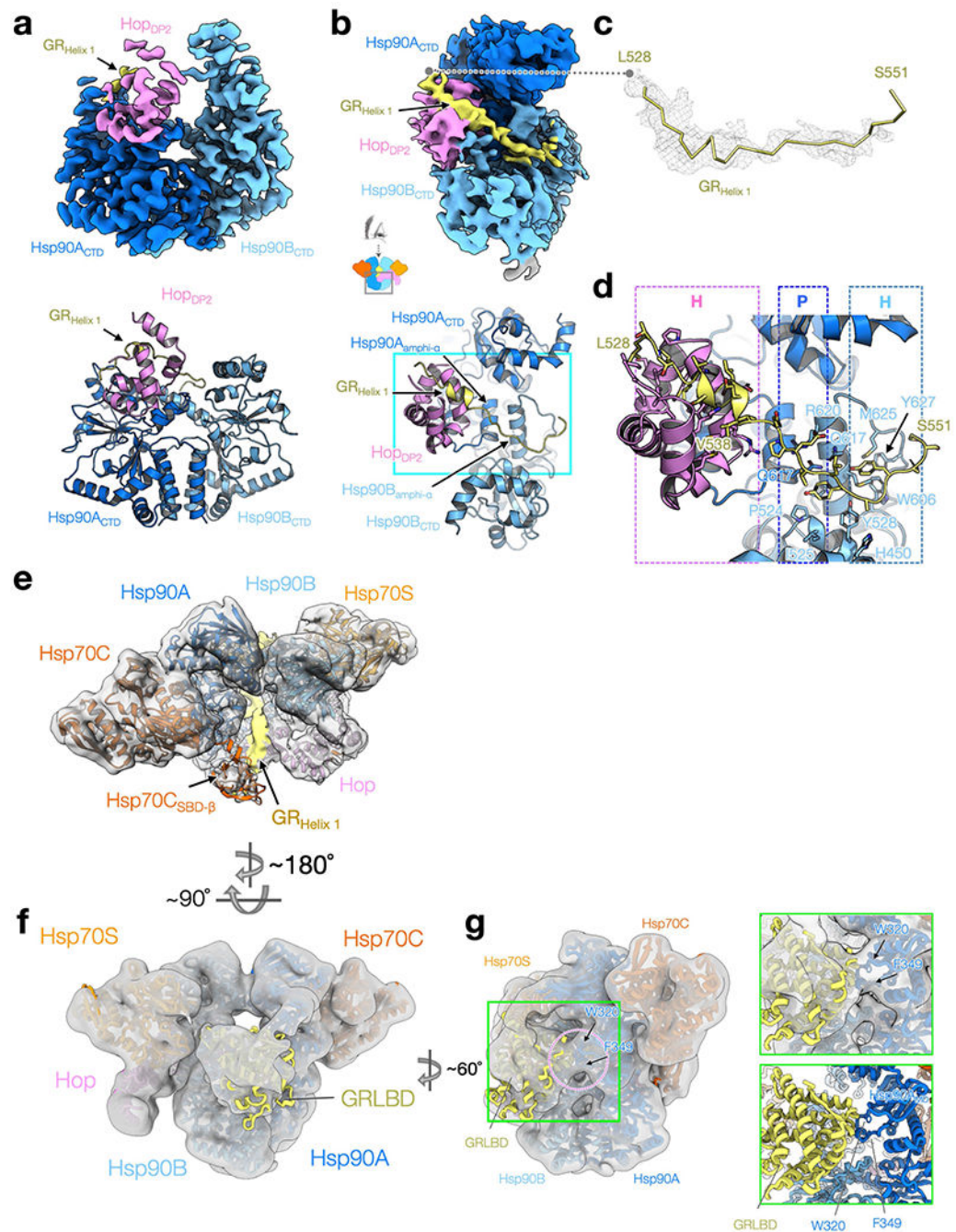
**Extended Data Fig. 7 |. The cryo-EM density and atomic model of GR$_{\text{Helix 1}}$ motif interacting with Hop$_{\text{DP2}}$.**

a, The focused map of the Hsp90AB$_{\text{CTD}}$:Hsp70C$_{\text{SBD-}\beta}$:Hop$^{\text{DP2}}$:GR$_{\text{Helix1}}$ (top) and the atomic model shown in ribbon representation (bottom). **b**, The top view of the reconstruction and model shown in **a**. **c**, The density (mesh) for the GR$_{\text{Helix 1}}$ motif (residues 528-551) gripped by Hsp90 and Hop$_{\text{DP2}}$. **d**, The atomic interactions of the GR$_{\text{Helix 1}}$ motif with Hsp90 and Hop$_{\text{DP2}}$ corresponding to **b**, cyan box in bottom). Residues in contact with the GR motif are shown in stick representation. The types of molecular interaction Hsp90 and

Hop_{DP2} provide are indicated at the top; H and P denote hydrophobic and polar interactions, respectively. **e**, The 7Å low-pass filtered cryo-EM map shows that the lumen density (yellow shade) of GR connects to the globular part of GR on the other side of Hsp90. **f**, Docking of the GRLBD to the 10Å low-pass filtered map shows that the low-resolution GR density can fit the rest of the GRLBD. **g**, The low-pass filtered map shows that W320 and F349 (arrows) of Hsp90A in the loading complex are in contact with GRLBD.
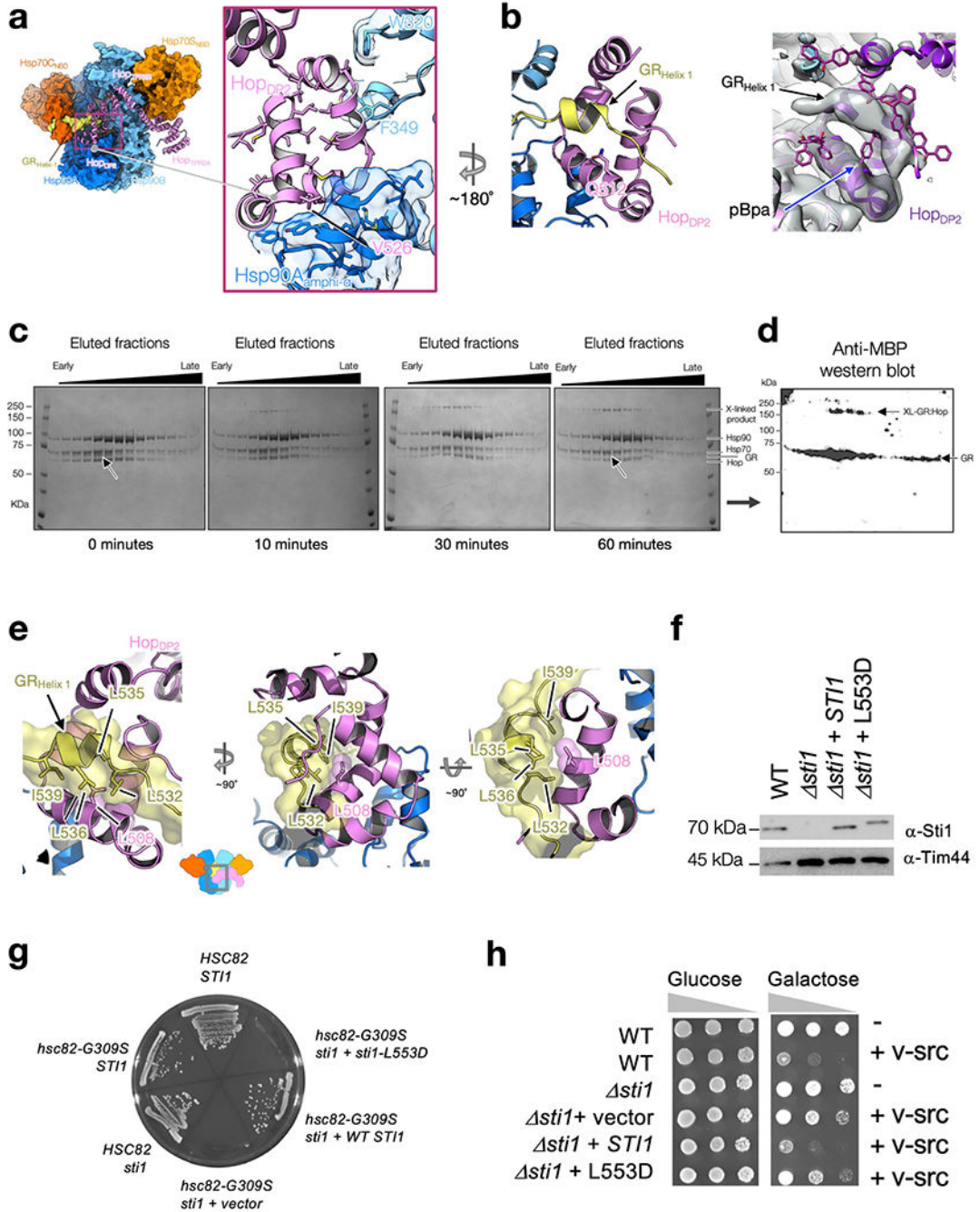
Extended Data Fig. 8 |. Validations of Hop_{DP2} binding to GR and of the in vivo importance of the client-binding pocket in HopDP2.

a–d, Using photoreactive, site-directed cross-linking to validate the Hop_{DP2}:GR interaction (**a**, the pink box) and (**b**, left). In **a**, Hop_{DP2} is loosely packed and uses surface-exposed hydrophobic residues, shown in sticks, to interact with $Hsp90A_{amphi-\alpha}$ (shown in transparent surface and with hydrophobic residues in sticks) and $Hsp90B^{W320,F349}$. Suggested by modelling of the photoreactive cross-linker *p*-benzoyl-L-phenylalanine (pBpa) on various positions of Hop_{DP2} to search for the position which is at the closest proximity to the GR_{Helix1} density (**b**, right), the pBpa was placed at Hop^{Q512} (**b**, left). The blue arrow on the right panel in **b** points at the selected position, Q512 (right panel, **b**). A time course of UV-exposed GR-loading complex analysed by SDS–PAGE and visualized by Coomassie staining (**c**). Whole fractions of GR-loading complex eluted from the size-exclusion column were exposed to UV using a gel imager (see also Methods). In **c**, arrows at 0 and 60 min indicate a reduced intensity of the GR band over the time course. Western blot of the SDS–PAGE gel after a 60 min UV exposure, using anti-MBP antibody to detect the MBP-tagged GR is shown in (**d**). Data in (**c, d**) are from one experiment. **e–h,** Hop_{DP2}'s client-binding/transfer function is crucial for cellular functions and client maturation. $Hop^{L508\ (L553\ in\ Sti1)}$ is located on the hydrophobic palm (Fig. 2d) of Hop^{DP2}, interacting closely with the LXXLL motif of $GR_{Helix\ 1}$ through hydrophobic interactions (**e**, left, middle and right). Mutations of Hop^{L508} completely abrogated GR function in vivo ($Sti1^{L553A}$ in Schmid et al. 2012[33]), lead to growth defects (**g**), and failed to promote v-src maturation (**h**). The mutant $Sti1^{L553D}$ accumulates at levels similar to WT Sti1 (**f**); data in **f** are from two independent experiments (see also Supplementary Fig. 10 for the uncropped gels/blots). Extracts from WT cells (JJ762), sti1 cells (JJ623) or sti1 cells transformed with a plasmid that expresses WT Sti1 or $Sti1^{L553D}$ were analysed by SDS–PAGE and immunoblotted with a polyclonal antisera specific for Sti1. Loading control is antibody against mitochondrial protein Tim44. In **g**, *sti1-L553D* is inviable in *hsc82hsp82* cells expressing *hsc82-G309S*. *hsc82hsp82* (JJ117) or *sti1hsc82hsp82* (JJ1443) strains harbouring YEp24-*HSP82* were transformed with plasmids expressing WT *HSC82* or *hsc82-G309S*. Strains that lacked *STI1* were also transformed with an empty plasmid or a plasmid expressing WT *STI1* or *sti1-L553D*. Transformants were grown in the presence of 5-FOA for 3 days to counter-select for the YEp24-*HSP82* plasmid. *STI1* is essential under these conditions and the growth of cells expressing *sti1-L553D* was indistinguishable from those expressing the empty plasmid. In **h**, WT cells, *sti1* cells or *sti1* cells transformed with a plasmid that expresses WT Sti1 or Sti1-L553D were transformed with an empty plasmid or a plasmid that expresses GAL-v-src. v-src induction in the presence of galactose sharply reduces the growth of WT cells, but not cells lacking *STI1*. The growth of cells expressing *sti1-L553D* was very similar to those expressing the empty plasmid, indicating that *sti1-L553D* is unable to support v-src function. The growth of cells in the presence of glucose was indistinguishable. 10-fold serial dilutions of cultures were grown for 3 days in the presence of galactose or glucose.
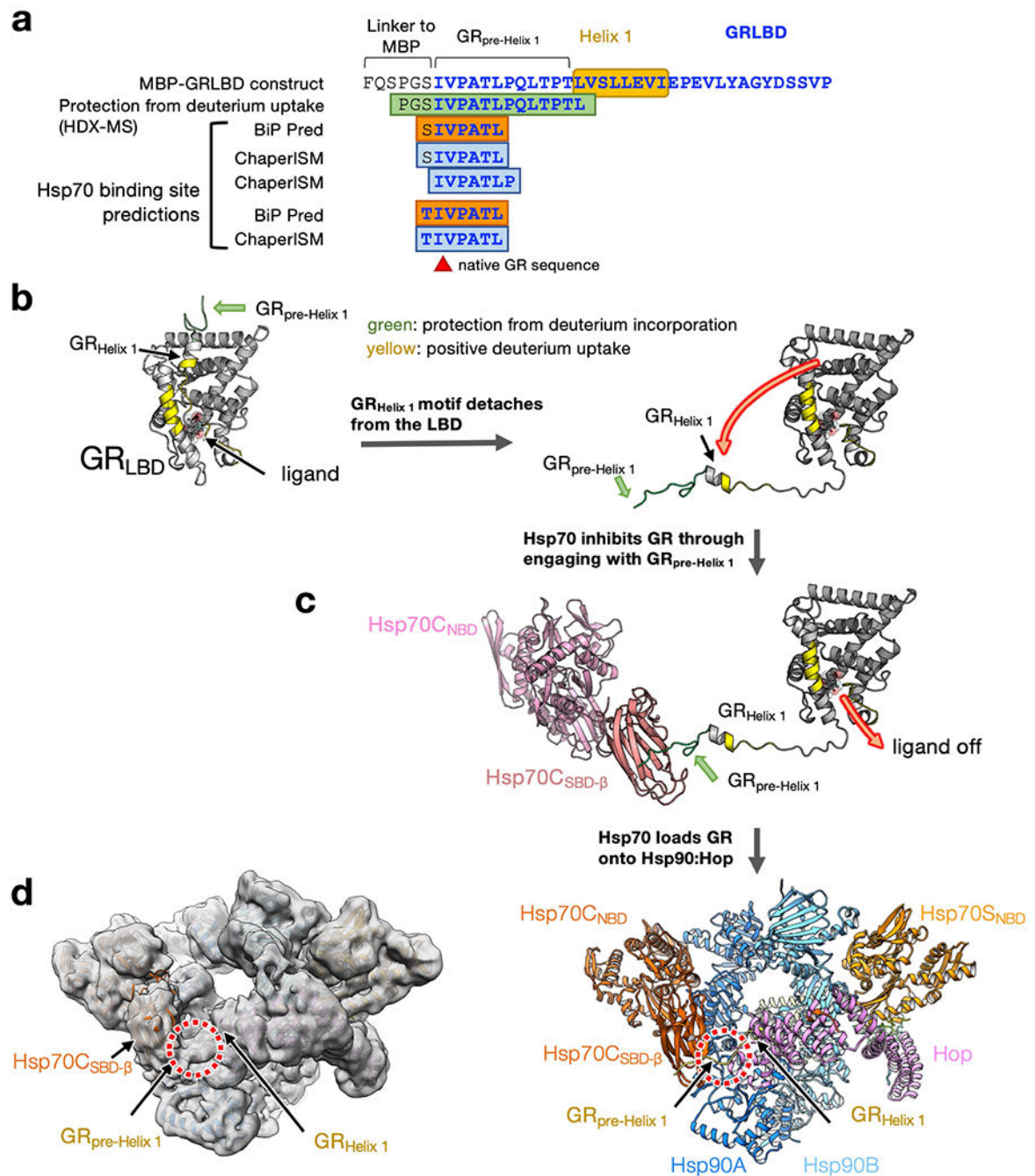
Extended Data Fig. 9 |. Hsp70 inhibits GR by binding the pre-Helix 1 region of GR.
a, After engaging with Hsp70/Hsp40, the GR$_{pre-Helix 1}$ region exhibits protection from deuterium incorporation in a HD-exchange mass spectrometry (HDX-MS) experiment8. In the GR$_{pre-Helix 1}$ region, there are Hsp70-binding sites predicted by two state-of-the-art algorithms (BiP Pred58 and ChaperISM59). **b**, Left, GRLBD crystal structure (PDB ID: 1M2Z) coloured by the change of deuterium uptake (HDX-MS data was retrieved from a previous study)8; green: protection from deuterium incorporation; yellow: positive deuterium uptake. Right, the detachment of the entire GR$_{Helix 1}$ motif explains the positive

deuterium uptake around the ligand-binding pocket. **c**, The protection from deuterium incorporation of the GR$_{pre\text{-}Helix\ 1}$ region can be explained by the binding of Hsp70. Together **b** and **c** provide a molecular mechanism describing how Hsp70 can inhibit GR ligand binding. **d**, GR's pre-Helix 1 remains bound to Hsp70C$_{SBD\text{-}\beta}$ (red circles) in the loading complex. Left, the 6Å; low-pass filtered cryo-EM map of the loading complex. Right, atomic model with ribbon presentation.
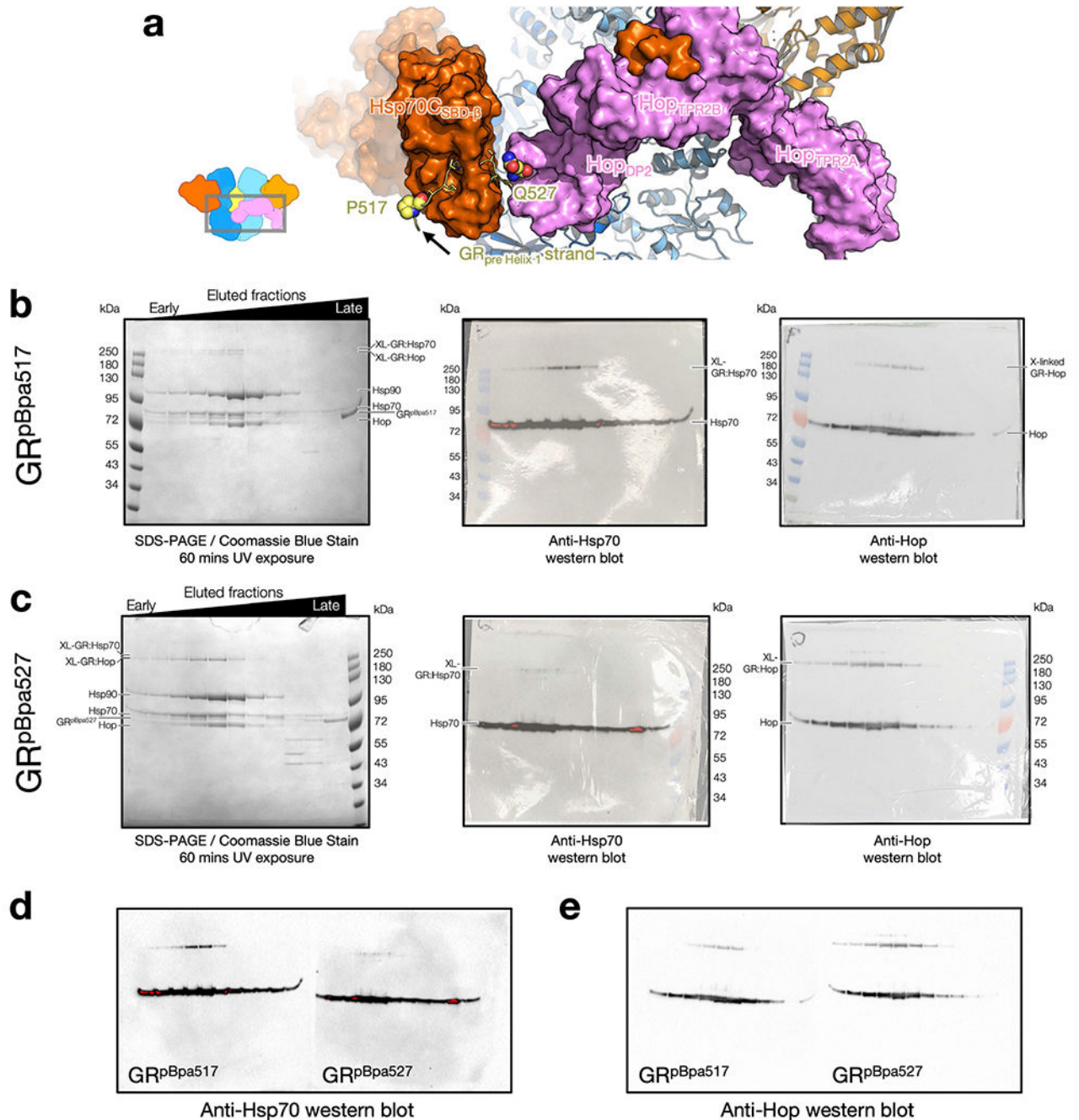
Extended Data Fig. 10 |. The GR$_{pre\text{-}Helix1}$ strand is engaged with the client-loading Hsp70 (Hsp70C) in the GR-loading complex.

a, The photoreactive cross-linker (pBpa) was placed at two positions in the $GR_{pre-Helix1}$ strand, residues before (GR^{P517}, sphere presentation) and after (GR^{Q527}, sphere representation) the predicted Hsp70-binding site ($GR^{519-526}$, stick representation). **b**, **c**, Whole fractions of GR-loading complex eluted from the size-exclusion column were exposed to UV using a gel imager (see also Methods). As expected, at both positions, cross-links between GR and Hsp70 were formed in the GR-loading complex, indicated by high molecular weight species. Left, SDS–PAGE stained with Coomassie blue. Middle, anti-Hsp70 Western blot. Right, anti-Hop Western blot. Data from (**b**, **c**) are from one experiment. Hsp70 cross-linking efficiency was higher for the $GR^{pBpa517}$ position (**b**, middle) than for the $GR^{pBpa527}$ position (**c**, middle). It is likely because 1) the C-terminal end of the Hsp70-bound substrate tends to be flexible in the reverse binding mode, as indicated by high atomic B-factors and missing density from previously determined Hsp70 crystal structures with a reverse peptide bound (PDB ID: 4EZZ, 4EZQ, 4EZT, and 4EZY)60, and 2) GR^{527} is closer to Hop^{543} than Hsp70. In addition, the two positions were able to cross-link with Hop (**b**, **c**, right), indicating it is the client-loading Hsp70 that the $GR_{pre-Helix 1}$ strand cross-linked with, rather than the scaffolding Hsp70. Note that although the GR^{517} position is not adjacent to Hop in the GR-loading complex model, we reasoned that the cross-link may be formed in the one-Hsp70 loading complex (**b**, right). These results demonstrate that it is the $GR_{pre-Helix 1}$ strand bound to Hsp70C, supporting our structural model. **d**, **e**, Raw western blots from middle and right panels in **b**, **c**. Red pixels in the western blots shown indicate overexposure.

Supplementary Material

Refer to Web version on PubMed Central for supplementary material.

Acknowledgements

Data availability

The electron microscopy maps and atomic model have been deposited into the Electron Microscopy Data Bank (EMDB) and the PDB. The accession codes for the GR-loading complex are EMD-23050 and 7KW7. Focused maps used for model refinements were also deposited with accession codes denoted in Supplementary Table 2 (EMD-23051, EMD-23053, EMD-23054, EMD-23055 and EMD-23056).

References

1. Kim YE, Hipp MS, Bracher A, Hayer-Hartl M & Hartl FU Molecular chaperone functions in protein folding and proteostasis. Annu. Rev. Biochem 82, 323–355 (2013). [PubMed: 23746257]

2. Genest O, Wickner S & Doyle SM Hsp90 and Hsp70 chaperones: collaborators in protein remodeling. J. Biol. Chem 294, 2109–2120 (2019). [PubMed: 30401745]

3. Lorenz OR et al. Modulation of the Hsp90 chaperone cycle by a stringent client protein. Mol. Cell 53, 941–953 (2014). [PubMed: 24613341]

4. Picard D et al. Reduced levels of hsp90 compromise steroid receptor action in vivo. Nature 348, 166–168 (1990). [PubMed: 2234079]

5. Nathan DF, Vos MH & Lindquist S In vivo functions of the *Saccharomyces cerevisiae* Hsp90 chaperone. Proc Natl Acad. Sci. USA 94, 12949–12956 (1997). [PubMed: 9371781]

6. Smith DF & Toft DO Minireview: the intersection of steroid receptors with molecular chaperones: observations and questions. Mol. Endocrinol 22, 2229–2240 (2008). [PubMed: 18451092]

7. Pratt WB, Morishima Y, Murphy M & Harrell M in Molecular Chaperones in Health and Disease (eds Starke K & Gaestel M) 111–138 (2006).

8. Kirschke E, Goswami D, Southworth D, Griffin PR & Agard DA Glucocorticoid receptor function regulated by coordinated action of the Hsp90 and Hsp70 chaperone cycles. Cell 157, 1685–1697 (2014). [PubMed: 24949977]

9. Noddings C, Wang RY-R, Johnson JL & Agard DA Structure of Hsp90–p23–GR reveals the Hsp90 client-remodelling mechanism. Nature 10.1038/s41586-021-04236-1 (2021).

10. Rosenzweig R, Nillegoda NB, Mayer MP & Bukau B The Hsp70 chaperone network. Nat. Rev. Mol. Cell Biol 20, 665–680 (2019). [PubMed: 31253954]

11. Taipale M, Jarosz DF & Lindquist S HSP90 at the hub of protein homeostasis: emerging mechanistic insights. Nat. Rev. Mol. Cell Biol 11, 515–528 (2010). [PubMed: 20531426]

12. Whitesell L & Lindquist SL HSP90 and the chaperoning of cancer. Nat. Rev. Cancer 5, 761–772 (2005). [PubMed: 16175177]

13. Lackie RE et al. The Hsp70/Hsp90 chaperone machinery in neurodegenerative diseases. Front. Neurosci 11, 254 (2017). [PubMed: 28559789]

14. Mayer MP & Gierasch LM Recent advances in the structural and mechanistic aspects of Hsp70 molecular chaperones. J. Biol. Chem 294, 2085–2097 (2019). [PubMed: 30455352]

15. Krukenberg KA, Street TO, Lavery LA & Agard DA Conformational dynamics of the molecular chaperone Hsp90. Q. Rev. Biophys 44, 229–255 (2011). [PubMed: 21414251]

16. Schopf FH, Biebl MM & Buchner J The HSP90 chaperone machinery. Nat. Rev. Mol. Cell Biol 18, 345–360 (2017). [PubMed: 28429788]

17. Boysen M, Kityk R & Mayer MP Hsp70- and Hsp90-mediated regulation of the conformation of p53 DNA binding domain and p53 cancer variants. Mol. Cell 74, 831–843 (2019). [PubMed: 31027880]

18. Dahiya V et al. Coordinated conformational processing of the tumor suppressor protein p53 by the Hsp70 and Hsp90 chaperone machineries. Mol. Cell 74, 816–830 (2019). [PubMed: 31027879]

19. Moran Luengo T, Kityk R, Mayer MP & Rudiger SGD Hsp90 breaks the deadlock of the Hsp70 chaperone system. Mol. Cell 70, 545–552 (2018). [PubMed: 29706537]

20. Morgner N et al. Hsp70 forms antiparallel dimers stabilized by post-translational modifications to position clients for transfer to Hsp90. Cell Rep. 11, 759–769 (2015). [PubMed: 25921532]

21. Nathan DF & Lindquist S Mutational analysis of Hsp90 function: interactions with a steroid receptor and a protein kinase. Mol. Cell. Biol 15, 3917–3925 (1995). [PubMed: 7791797]

22. Bohen SP & Yamamoto KR Isolation of Hsp90 mutants by screening for decreased steroid receptor function. Proc. Natl Acad. Sci. USA 90, 11424–11428 (1993). [PubMed: 8248264]

23. Kravats AN et al. Functional and physical interaction between yeast Hsp90 and Hsp70. Proc. Natl Acad. Sci. USA 115, E2210–E2219 (2018). [PubMed: 29463764]

24. Doyle SM et al. Intermolecular interactions between Hsp90 and Hsp70. J. Mol. Biol 431, 2729–2746 (2019). [PubMed: 31125567]

25. Genest O, Hoskins JR, Kravats AN, Doyle SM & Wickner S Hsp70 and Hsp90 of *E. coli* directly interact for collaboration in protein remodeling. J. Mol. Biol 427, 3877–3889 (2015). [PubMed: 26482100]

26. Flynn JM et al. Comprehensive fitness maps of Hsp90 show widespread environmental dependence. eLife 9, e58310 (2020).

27. Genest O, Hoskins JR, Camberg JL, Doyle SM & Wickner S Heat shock protein 90 from *Escherichia coli* collaborates with the DnaK chaperone system in client protein remodeling. Proc. Natl Acad. Sci. USA 108, 8206–8211 (2011). [PubMed: 21525416]

28. Sung N et al. 2.4 A resolution crystal structure of human TRAP1NM, the Hsp90 paralog in the mitochondrial matrix. Acta Crystallogr. D 72, 904–911 (2016).

29. Sun M, Kotler JLM, Liu S & Street TO The endoplasmic reticulum (ER) chaperones BiP and Grp94 selectively associate when BiP is in the ADP conformation. J. Biol. Chem 294, 6387–6396 (2019). [PubMed: 30787103]

30. Kirschke E, Roe-Zurz Z, Noddings C & Agard D The interplay between Bag-1, Hsp70, and Hsp90 reveals that inhibiting Hsp70 rebinding is essential for glucocorticoid receptor activity. Preprint at 10.1101/2020.05.03.075523 (2020).

31. Mandal AK et al. Hsp110 chaperones control client fate determination in the hsp70-Hsp90 chaperone system. Mol. Biol. Cell 21, 1439–1448 (2010). [PubMed: 20237159]

32. Sahasrabudhe P, Rohrberg J, Biebl MM, Rutz DA & Buchner J The plasticity of the Hsp90 co-chaperone System. Mol. Cell 67, 947–961 (2017). [PubMed: 28890336]

33. Schmid AB et al. The architecture of functional modules in the Hsp90 co-chaperone Sti1/Hop. EMBO J. 31, 1506–1517 (2012). [PubMed: 22227520]

34. Southworth DR & Agard DA Client-loading conformation of the Hsp90 molecular chaperone revealed in the cryo-EM structure of the human Hsp90:Hop complex. Mol. Cell 42, 771–781 (2011). [PubMed: 21700222]

35. Lee CT, Graf C, Mayer FJ, Richter SM & Mayer MP Dynamics of the regulation of Hsp90 by the co-chaperone Sti1. EMBO J. 31, 1518–1528 (2012). [PubMed: 22354036]

36. Reidy M, Kumar S, Anderson DE & Masison DC Dual roles for yeast Sti1/Hop in regulating the Hsp90 chaperone cycle. Genetics 209, 1139–1154 (2018). [PubMed: 29930177]

37. Verba KA et al. Atomic structure of Hsp90–Cdc37–Cdk4 reveals that Hsp90 traps and stabilizes an unfolded kinase. Science 352, 1542–1547 (2016). [PubMed: 27339980]

38. Suren T et al. Single-molecule force spectroscopy reveals folding steps associated with hormone binding and activation of the glucocorticoid receptor. Proc. Natl Acad. Sci. USA 115, 11688–11693 (2018). [PubMed: 30366952]

39. Bohen SP Hsp90 mutants disrupt glucocorticoid receptor ligand binding and destabilize aporeceptor complexes. J. Biol. Chem 270, 29433–29438 (1995). [PubMed: 7493981]

40. Hawle P et al. The middle domain of Hsp90 acts as a discriminator between different types of client proteins. Mol. Cell. Biol 26, 8385–8395 (2006). [PubMed: 16982694]

41. Genest O et al. Uncovering a region of heat shock protein 90 important for client binding in E. coli and chaperone function in yeast. Mol. Cell 49, 464–473 (2013). [PubMed: 23260660]

42. Liu Y et al. Cryo-EM structures reveal a multistep mechanism of Hsp90 activation by co-chaperone Aha1. Preprint at 10.1101/2020.06.30.180695 (2020).

43. Rutz DA et al. A switch point in the molecular chaperone Hsp90 responding to client interaction. Nat. Commun 9, 1472 (2018). [PubMed: 29662162]

44. Li C et al. FastCloning: a highly simplified, purification-free, sequence- and ligation-independent PCR cloning method. BMC Biotechnol. 11, 92 (2011). [PubMed: 21992524]

45. Chin JW, Martin AB, King DS, Wang L & Schultz PG Addition of a photocrosslinking amino acid to the genetic code of *Escherichia coli*. Proc. Natl. Acad. Sci. USA 99, 11020–11024 (2002). [PubMed: 12154230]

46. Obermann WM, Sondermann H, Russo AA, Pavletich NP & Hartl FU In vivo function of Hsp90 is dependent on ATP binding and ATP hydrolysis. J. Cell Biol 143, 901–910 (1998). [PubMed: 9817749]

47. Schorb M, Haberbosch I, Hagen WJH, Schwab Y & Mastronarde DN Software tools for automated transmission electron microscopy. Nat. Methods 16, 471–477 (2019). [PubMed: 31086343]

48. Zheng SQ et al. MotionCor2: anisotropic correction of beam-induced motion for improved cryo-electron microscopy. Nat. Methods 14, 331–332 (2017). [PubMed: 28250466]

49. Rohou A & Grigorieff N CTFFIND4: fast and accurate defocus estimation from electron micrographs. J. Struct. Biol 192, 216–221 (2015). [PubMed: 26278980]

50. Scheres SH RELION: implementation of a Bayesian approach to cryo-EM structure determination. J. Struct. Biol 180, 519–530 (2012). [PubMed: 23000701]

51. Zivanov J et al. New tools for automated high-resolution cryo-EM structure determination in RELION-3. Elife 7, e42166 (2018). [PubMed: 30412051]

52. Bai XC, Rajendra E, Yang G, Shi Y & Scheres SH Sampling the conformational space of the catalytic subunit of human gamma-secretase. Elife 4, e11182 (2015). [PubMed: 26623517]

53. Leman JK et al. Macromolecular modeling and design in Rosetta: recent methods and frameworks. Nat. Methods 17, 665–680 (2020). [PubMed: 32483333]

54. Li J et al. Structure insights into mechanisms of ATP hydrolysis and the activation of human heat-shock protein 90. Acta Biochim Biophys Sin 44, 300–306 (2012). [PubMed: 22318716]

55. Arakawa A, Handa N, Shirouzu M & Yokoyama S Biochemical and structural studies on the high affinity of Hsp70 for ADP. Protein Sci. 20, 1367–1379 (2011). [PubMed: 21608060]

56. Zhang P, Leu JI, Murphy ME, George DL & Marmorstein R Crystal structure of the stress-inducible human heat shock protein 70 substrate-binding domain in complex with peptide substrate. PLoS ONE 9, e103518 (2014). [PubMed: 25058147]

57. Wang RY et al. De novo protein structure determination from near-atomic-resolution cryo-EM maps. Nat. Methods 12, 335–338 (2015). [PubMed: 25707029]

58. Schneider M et al. BiPPred: combined sequence- and structure-based prediction of peptide binding to the Hsp70 chaperone BiP. Proteins 84, 1390–1407 (2016). [PubMed: 27287023]

59. Gutierres MBB, Bonorino CBC & Rigo MM ChaperISM: improved chaperone binding prediction using position-independent scoring matrices. Bioinformatics 36, 735–741 (2020). [PubMed: 31504177]

60. Zahn M et al. Structural studies on the forward and reverse binding modes of peptides to the chaperone DnaK. J. Mol. Biol 425, 2463–2479 (2013). [PubMed: 23562829]

61. Soding J, Biegert A & Lupas AN The HHpred interactive server for protein homology detection and structure prediction. Nucleic Acids Res. 33, W244–W248 (2005). [PubMed: 15980461]

62. Song Y et al. High-resolution comparative modeling with RosettaCM. Structure 21, 1735–1742 (2013). [PubMed: 24035711]

63. Darby JF et al. Solution structure of the Hop TPR2A domain and investigation of target druggability by NMR, biochemical and in silico approaches. Sci. Rep 10, 16000 (2020). [PubMed: 32994435]

64. DiMaio F, Zhang J, Chiu W & Baker D Cryo-EM model validation using independent map reconstructions. Protein Sci. 22, 865–868 (2013). [PubMed: 23592445]

65. Wang RY et al. Automated structure refinement of macromolecular assemblies from cryo-EM maps using Rosetta. Elife 5, e17219 (2016). [PubMed: 27669148]

66. Bledsoe RK et al. Crystal structure of the glucocorticoid receptor ligand binding domain reveals a novel mode of receptor dimerization and coactivator recognition. Cell 110, 93–105 (2002). [PubMed: 12151000]

67. Liu XD, Morano KA & Thiele DJ The yeast Hsp110 family member, Sse1, is an Hsp90 cochaperone. J. Biol. Chem 274, 26654–26660 (1999). [PubMed: 10480867]

68. Sondermann H et al. Structure of a Bag/Hsc70 complex: convergent functional evolution of Hsp70 nucleotide exchange factors. Science 291, 1553–1557 (2001). [PubMed: 11222862]

69. Polier S, Dragovic Z, Hartl FU & Bracher A Structural basis for the cooperation of Hsp70 and Hsp110 chaperones in protein folding. Cell 133, 1068–1079 (2008). [PubMed: 18555782]

70. Johnson JL, Halas A & Flom G Nucleotide-dependent interaction of *Saccharomyces cerevisiae* Hsp90 with the cochaperone proteins Sti1, Cpr6, and Sba1. Mol. Cell. Biol 27, 768–776 (2007). [PubMed: 17101799]

71. Flom G, Weekes J, Williams JJ & Johnson JL Effect of mutation of the tetratricopeptide repeat and asparatate-proline 2 domains of Sti1 on Hsp90 signaling and interaction in *Saccharomyces cerevisiae*. Genetics 172, 41–51 (2006). [PubMed: 16219779]

72. Street TO et al. Elucidating the mechanism of substrate recognition by the bacterial Hsp90 molecular chaperone. J. Mol. Biol 426, 2393–2404 (2014). [PubMed: 24726919]

73. Kityk R, Kopp J & Mayer MP Molecular mechanism of J-domain-triggered ATP hydrolysis by Hsp70 chaperones. Mol. Cell 69, 227–237 e224 (2018). [PubMed: 29290615]

74. Dey B, Lightbody JJ & Boschelli F CDC37 is required for p60v-src activity in yeast. Mol. Biol. Cell 7, 1405–1417 (1996). [PubMed: 8885235]

75. Kityk R, Kopp J, Sinning I & Mayer MP Structure and dynamics of the ATP-bound open conformation of Hsp70 chaperones. Mol. Cell 48, 863–874 (2012). [PubMed: 23123194]
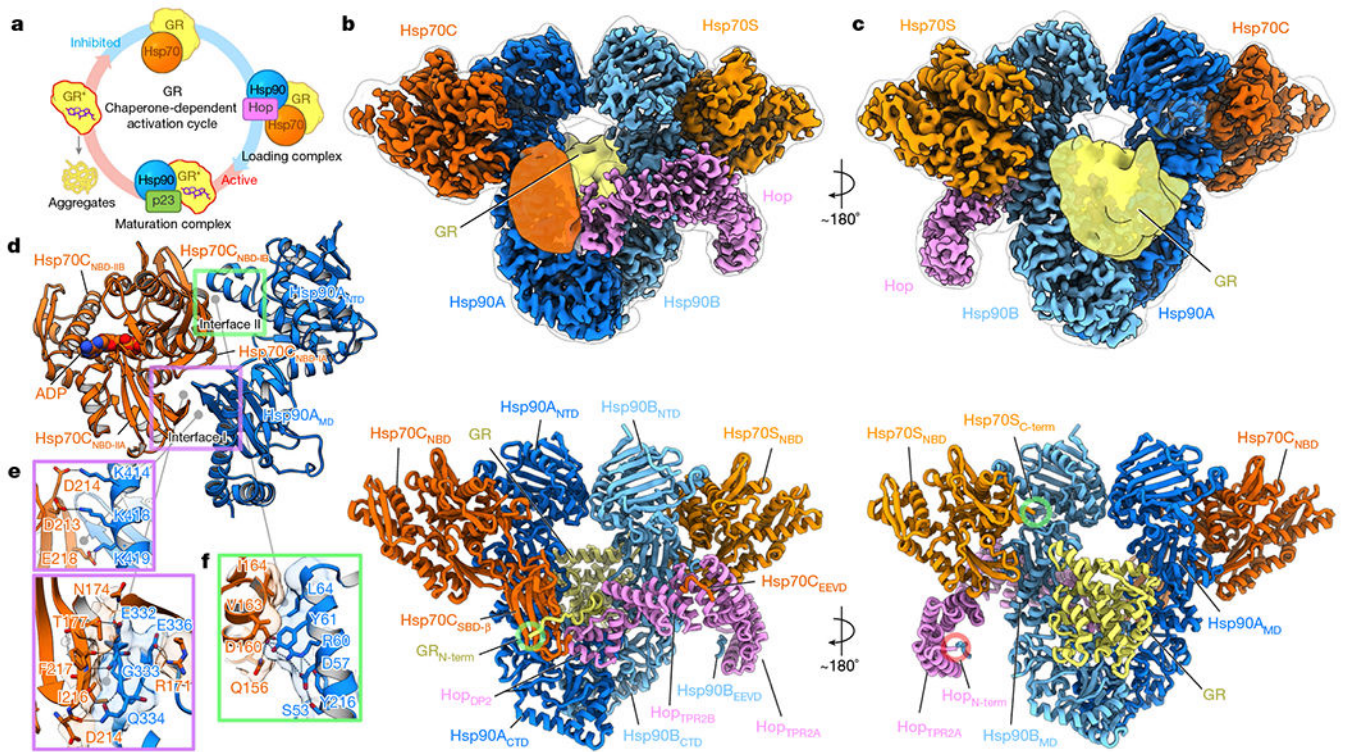
Fig. 1 |. GR-loading complex and the molecular basis of Hsp90–Hsp70 interactions.
a, GR ligand binding is regulated by molecular chaperones in a constant cycle of inactivation and activation. The activated states of GR are indicated by asterisks. **b**, **c**, Front (**b**) and back (**c**) views of a composite cryo-EM map and the atomic model of the GR-loading complex. Densities of $Hsp70C_{SBD}$ and the globular C-terminal GR are taken from the 10 Å low-pass-filtered map of the high-resolution reconstruction of the full complex. Subunit colouring is maintained throughout. **d**–**f**, Hsp90–Hsp70 interactions (**d**) are mediated via two main interfaces (interface I, purple rectangle (**e**) and interface II, green rectangle (**f**)). Residues involved in these interactions are shown in sticks and transparent surfaces(**e**, **f**). Dominant polar interactions are depicted by dashed lines.
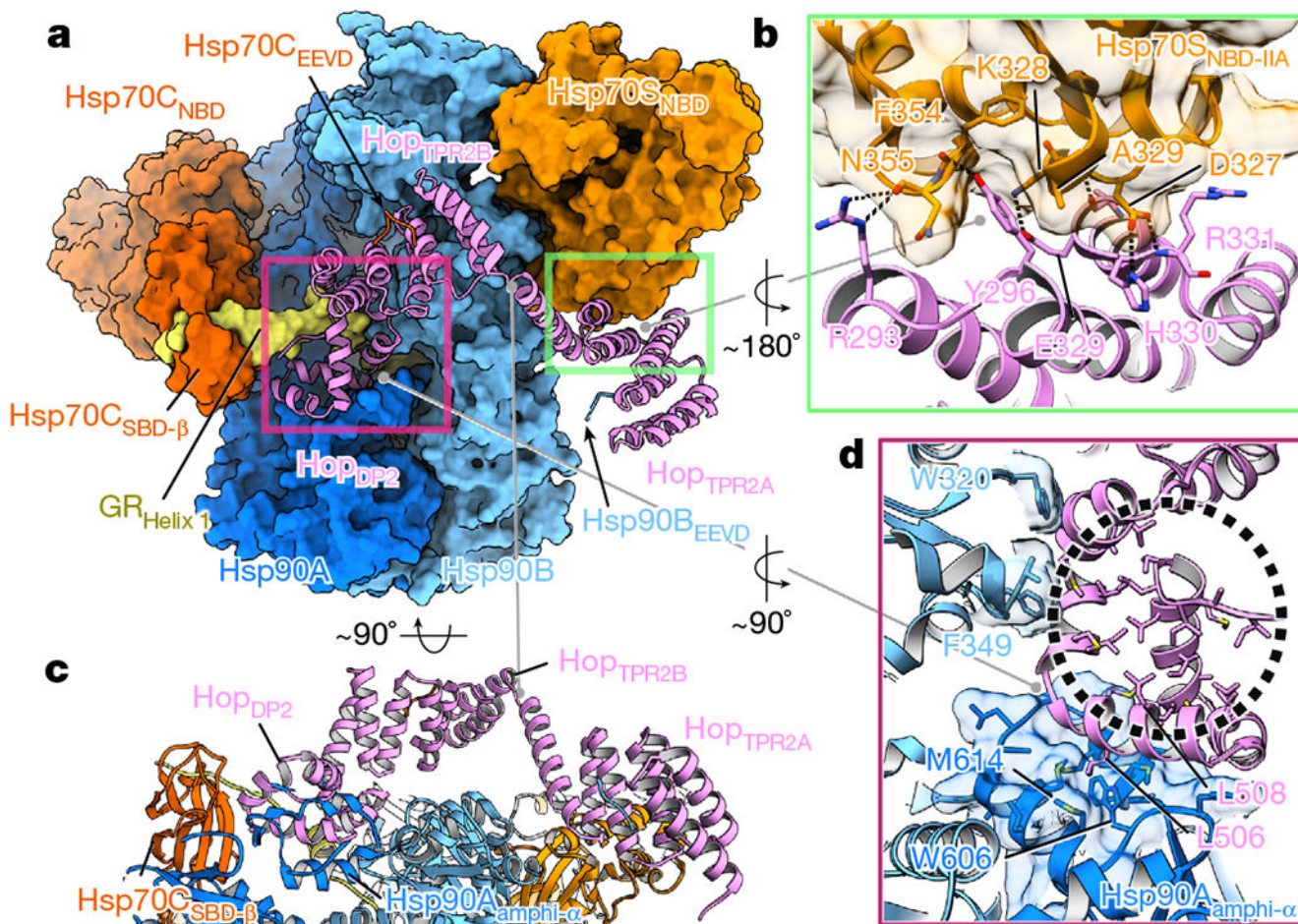
Fig. 2 |. Hop interacts closely with all components in the loading complex.
a, Hop (pink ribbon) uses Hop_{TPR2A} to interact with Hsp70S (green rectangle). Hop_{DP2} interacts with both Hsp90 protomers, Hsp70C_{SBD} and a portion of GR (pink rectangle). The Hop TPRs also bind EEVD fragments from both Hsp90 and Hsp70. **b**, In the Hop–Hsp70 interface (green rectangle, **a**), the Hop residue Y296 inserts into a cavity on Hsp70S_{NBD-IIA} (transparent surface). Dashed lines depict polar interactions. **c**, Hop_{TPR2B} is suspended above Hsp90, supported by Hsp70–Hop_{TPR2A} and Hsp90–Hop_{DP2}. **d**, Hop_{DP2} uses surface-exposed hydrophobic residues to interact with Hsp90A_{amphi-α} (shown with transparent surface and with hydrophobic residues in sticks) and Hsp90B(W320, F349). Hop_{DP2} is loosely packed with many hydrophobic residues exposed in the 'palm' (black circle) of the 'hand'. Note that the binding of GR to Hop_{DP2} is omitted.
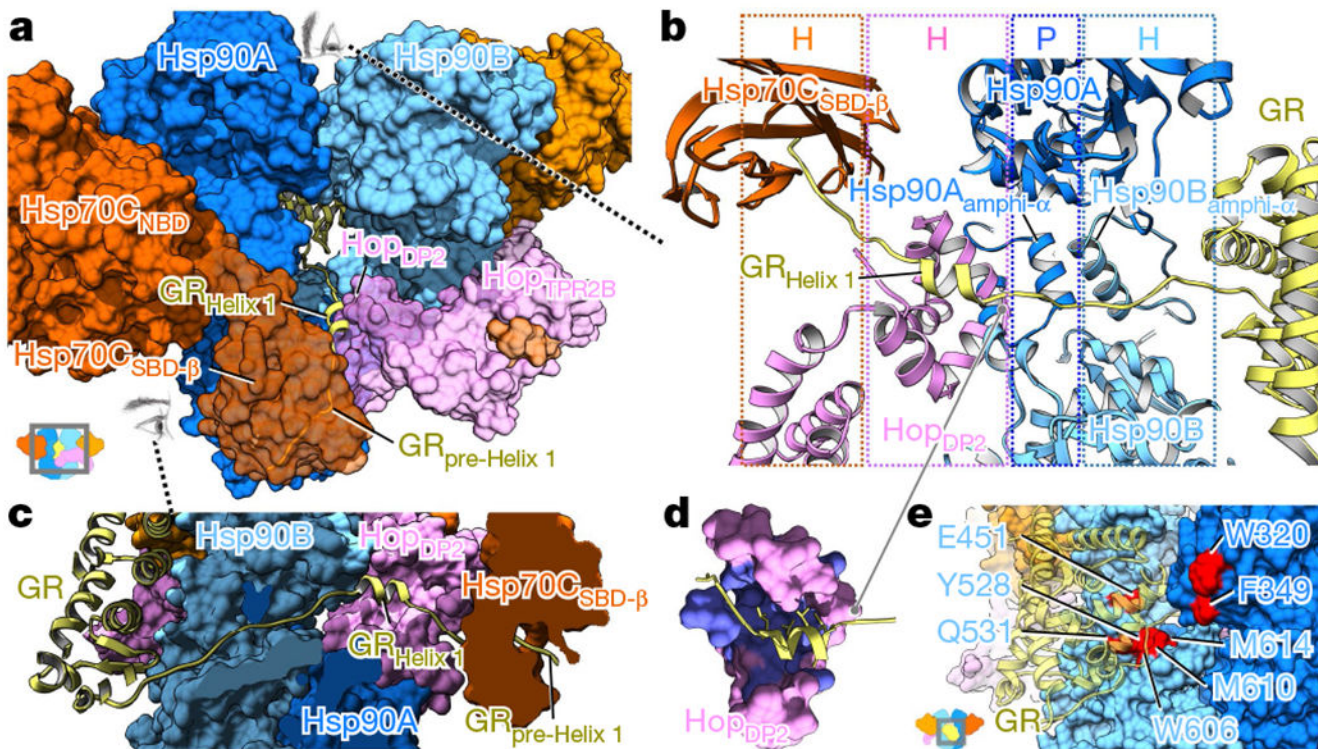
Fig. 3 |. GR is unfolded and threaded through the Hsp90 lumen, binding Hop$_{DP2}$ and Hsp70C$_{SBD-\beta}$.

a, GR (ribbon model) is partially unfolded, with the N-terminal residues simultaneously gripped by Hsp70C$_{SBD-\beta}$ and Hop$_{DP2}$, and is threaded through the semi-closed lumen of Hsp90. The remaining GR is at the other side of the loading complex, which was modelled by docking this portion (556–777) from the GR crystal structure into the 10 Å low-pass-filtered GR density (Methods). **b**, Top-down view of GR recognition via an extended client-binding pocket collectively formed by Hsp70C$_{SBD-\beta}$, Hop$_{DP2}$ and Hsp90A/B$_{amphi-\alpha}$s. The N-terminal residues of GR (residues 520–551), which form a strand-helix-strand motif (yellow), are captured in the loading complex. The molecular property of each binding pocket is colour-coded and labelled on the top panel (H and P denote hydrophobic and polar interactions, respectively). **c**, Side view (see-through) of the GR N-terminal motif captured by the loading complex. **d**, The exposed hydrophobic pocket in Hop$_{DP2}$ (purple) binds the LXXLL motif of GR$_{Helix1}$. **e**, Residues on Hsp90 (blue and cyan surface) previously reported to be important for GR (transparent yellow ribbon) activation are highlighted in red.
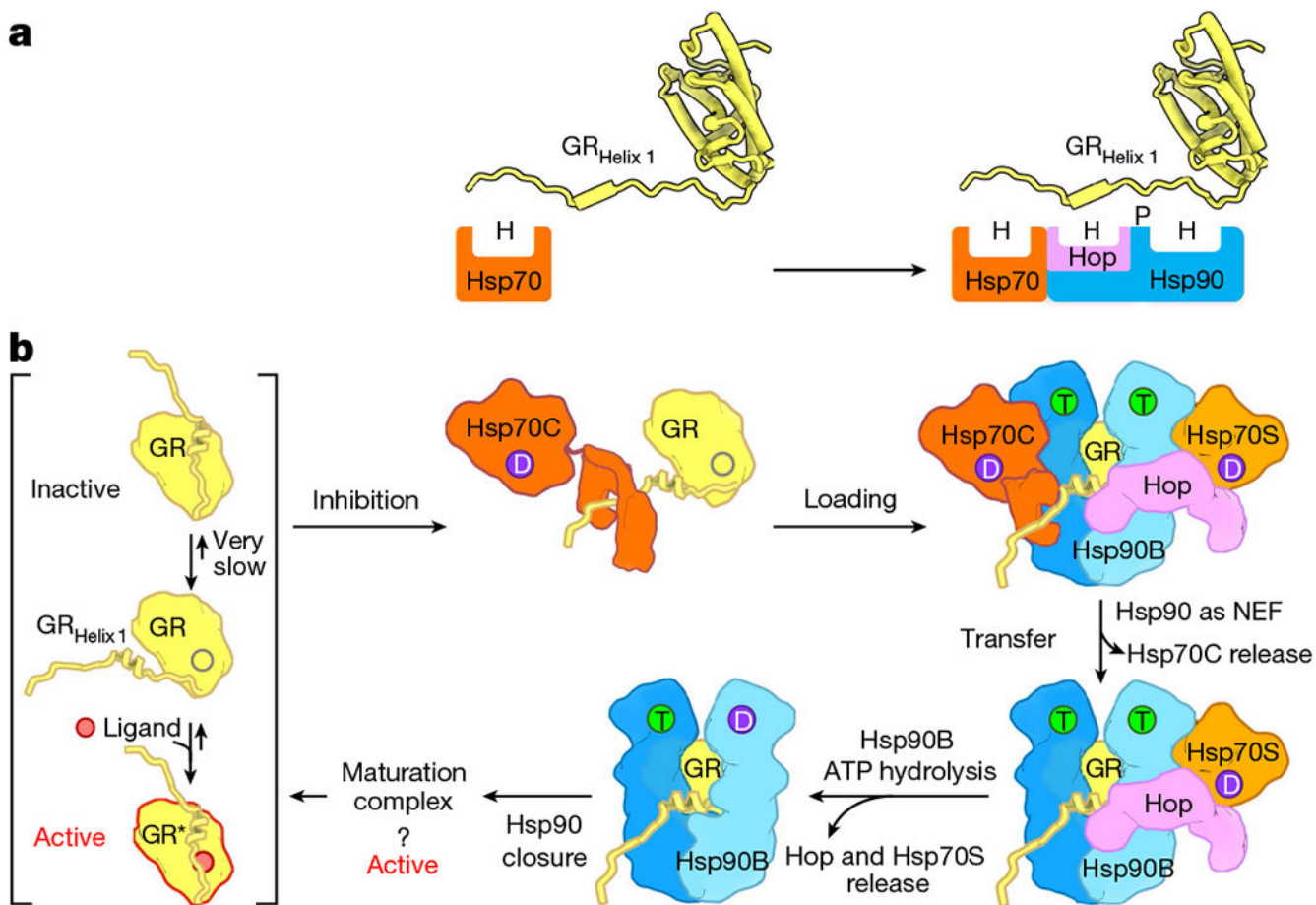
Fig. 4 |. Model of how Hsp70 loads GR onto Hsp90.

a, The molecular principle of GR recognition at the client-loading step. H and P denote hydrophobic and polar interactions, respectively. **b**, Catalysis of GR ligand binding by the actions of Hsp70 and Hsp90. GR under physiological conditions is in a sparingly populated equilibrium between apo-closed (inactive) and open apo states to which ligand can bind. $GR_{Helix\ 1}$ acts as a lid to gate and support ligand binding. Hsp70C (dark orange) in its ADP state (D) binds the $GR_{pre\text{-}Helix\ 1}$ strand, enabling $GR_{Helix\ 1}$ to detach and inhibit ligand binding (top middle). Facilitated by HopDP2 recognizing the $GR_{Helix\ 1}$ LXXLL motif, Hsp70C loads GR onto Hsp90 (blue), forming the client-loading complex (top right). Although the observed structure was for an Hsp90^{Apo} state, under physiological conditions ATP is highly abundant and would probably occupy Hsp90's ATP-binding pockets (T). The ATP binding and NEF activity of Hsp90 facilitate the release of Hsp70C (bottom right). The energy from the ATP hydrolysis (D) on Hsp90B (light blue) is used to release Hsp70S (light orange) and Hop (bottom middle), which is followed by full closure of Hsp90 towards the GR-maturation complex[9].